Journal Pre-proof

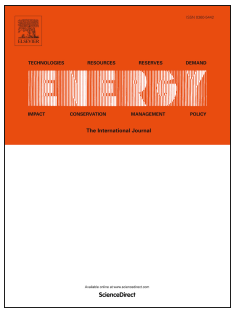

Modelling calcium looping at industrial scale for energy storage in concentrating solar power plants

Manuel Bailera, Sara Pascual, Pilar Lisbona, Luis M. Romeo

PII: S0360-5442(21)00555-7

DOI: https://doi.org/10.1016/j.energy.2021.120306

Reference: EGY 120306

To appear in: *Energy*

Received Date: 6 October 2020

Revised Date: 28 January 2021

Accepted Date: 4 March 2021

Please cite this article as: Bailera M, Pascual S, Lisbona P, Romeo LM, Modelling calcium looping at industrial scale for energy storage in concentrating solar power plants, *Energy*, https://doi.org/10.1016/j.energy.2021.120306.

Manuel Bailera: Conceptualization, Methodology, Software, Validation, Formal analysis, Writing – Original Draft, Writing – Review & Editing, Visualization. **Sara Pascual:** Conceptualization, Methodology, Software, Formal analysis, Writing – Original Draft, Writing – Review & Editing, Visualization. **Pilar Lisbona:** Conceptualization, Methodology, Writing – Original Draft, Writing – Review & Editing. **Luis M Romeo:** Conceptualization, Writing – Original Draft, Writing – Review & Editing, Funding acquisition.

Modelling calcium looping at industrial scale for energy storage in concentrating solar power plants

Manuel Bailera[a], Sara Pascual[a], Pilar Lisbona[b] and Luis M. Romeo[a]

[a] Escuela de Ingeniería y Arquitectura. Universidad de Zaragoza, Campus Río Ebro, María de Luna 3, 50018, Zaragoza, Spain

[b] Fundación Agencia Aragonesa para la Investigación y el Desarrollo (ARAID), Zaragoza, Spain

Abstract:

Ca-Looping represents one of the most promising technologies for thermochemical energy storage. This process based on the carbonation-calcination cycle of CaO offers a high potential to be coupled with solar power plants for its long-term storage capacity and high temperatures. Previous studies analyzed different configurations of CaL integrated into power cycles aiming to improve efficiency. However, most of these assessments based on lumped models did not account for scale effect in the most critical reactor. In this work, a detailed 1D-model of a large-scale carbonator is included in the comprehensive model of the integrated facility. The results obtained served to assess the available heat, the minimum technical part load of this equipment, the required size of the storage tanks and the overall efficiency of the plant. The main issue in the operation of large-size carbonator is the heat removal, thus a multi-tube internally cooled reactor is proposed. The designed carbonator provides 80 MWth at nominal operation and 40 MWth at minimum part load operation. The sizing of storage tanks depends on the operation management, ranging between 5,700-11,400 m^3 for 15 hours. Different efficiencies of the system were defined and presented through operating maps, as a function of the reactor loads.

Keywords:

Energy storage, Calcium looping, Concentrated solar power, CO2, Thermochemical energy storage

1. Introduction

Deploying renewable energy sources (RES) contributes to the decarbonisation of energy systems [1]. However, curtailments are necessary when RES represent above 10% of the annual electricity generation [2], since operators only control 5–10% of wind and solar dispatch [3]. To face this situation, the European Commission proposed energy storage as solution [4] since 10–20% variable RES shares are estimated for about 50 regions in the world by 2023 [5].

In this study, we focus on concentrating solar power (CSP) plants. Dispatch of CSP has a peak around noon and significant variations over minutes or hours due to cloud coverage. To manage electricity production, half of the CSP plants worldwide use thermal energy storage (TES) [6]. TES systems retain thermal energy within specific materials and release it when needed. According to the physical phenomena occurring while absorbing/releasing the energy, thermal energy storage is classified in sensible TES, latent TES and thermochemical energy storage (TCES).

Sensible TES use materials with high specific heat (131–4187 J/kg·K) to store/release the energy by heating/cooling their mass. These systems are simple, reliable and cheap, but the energy storage density is low (1001–4453 kJ/m^3·K) [7]. Most of sensible TES used in commercial CSP plants are based on molten salts [8], combining two tanks (packed beds) of high and low temperature for short- and long-term storage [9].

Latent TES use materials with high latent heat (112–260 kJ/kg), to store/release the energy during phase transitions at constant temperature, what reduces fluctuations in electricity production [7]. Phase change takes place between liquid and solid, in order to have small variations in volume (<10%) [10] and high energy storage densities (50 to 150 kWh/t). However, the low thermal conductivity of these materials (< 0.5 W/m·K) prolongs the time of charging and discharging energy [7]. To obtain large heat exchange surfaces in latent TES, shell and tubes configurations are commonly used [11][12].

Thermochemical energy storage systems are based upon reversible chemical reactions (endothermic in one direction and exothermic in the other) to store/release energy through a cyclic process. As TCES works at very high temperatures (450–1300 ºC), it is the most promising candidate for thermal energy storage in new generation CSP plants working above 800 ºC [7][13]. Moreover, TCES provides seasonal storage with no heat losses (the energy is stored in the chemical bound of the compounds) with higher energy densities than sensible and latent TES (about 240-1090 kWh/t) [14]. Among many materials for TCES (hydrides, metal oxides and carbonate salts), the calcium looping reaction (CaL), $CaO_3 \leftrightarrow CaO+CO_2$, stands out because the material is cheap and earth-abundant, products are non-toxic, and energy storage density reaches 390 kWh/t [14][15].

The utilization of CaL for TCES was proposed by Barker in 1974 [16], and the scientific community intensified its research during the last decade. Recently, several papers dealt with the integration of CaL TCES with different power cycles [17][18], efficiency optimization [19][20][21], and management of the storage system [22]. Ortiz et al. [17] and Tesio et al. [18] assessed different power plant options to find the technology that leads to better performance when integrated with calcium looping TCES. Both of them concluded that best results are achieved with CO_2 power cycles (CO_2 closed Brayton cycle according to Ortiz, and supercritical CO_2 power block according to Tesio). After identifying the most suitable technology, they optimized the efficiency of the concept by studying different plant layouts. They found overall efficiencies (net electric production to net solar thermal input) in the range 32-44% for the CO_2 closed Brayton cycle [19][20], and 40.4% for the supercritical CO_2 cycle [21]. Regarding management, Bravo et al. used a multi-objective optimization framework to determine the best operational strategy. However, authors state that further research on this issue is necessary to reach authoritative conclusions, as economic aspects were not included in the optimization [22].

So far, the reactors design has not been taken into account in the existing studies which are mainly based on lumped models of the process. However, the extension of the chemical reactions in the carbonator and calciner clearly affects the mass flows, the management of storages and the overall efficiency of the plant [14]. The main reason is that experiments on calcium looping applied to TCES are scarce making difficult the validation of detailed models of the reactors [23]. Solar calcination ($CaO_3 \rightarrow CaO+CO_2$, endothermic) has been tested by the Paul Scherrer Institute in a cyclone gas-particle separator with a window-less aperture. Solar thermal input of the prototype was 54 kW, reaching 85% limestone conversion with 88% energy efficiency [24]. Carbonation ($CaO+CO_2 \rightarrow CaO_3$, exothermic), within the framework of solar CaL, is tested in the SOCRATCES project. They use an entrained flow reactor of 10 kW thermal output, cooled by external cooling coils. The cooling fluid is air, which is later used in a Stirling engine to produce power [25].

At industrial scale, the computational fluid dynamics simulations of the Paul Scherrer Institute show that solar calcination may operate effectively at 55 MW thermal inputs by using a falling particle receiver. In this type of reactors, a curtain of falling $CaCO_3$ particles absorb the solar radiation that enters through the aperture of the receiver [24]. Regarding carbonation, Bailera et al. showed that energy could not be properly recovered in entrained flow reactors when scaled-up to industrial scale, if they are cooled by external coils. Since the reactor heats up, the reaction reaches the equilibrium temperature and it progresses limited by the rate at which heat is evacuated. This leads to unfeasible dimensions of reactors (7 m diameter and 52 m length for carbonators of 100 MW solar input) [26]. Therefore, other potential configurations must be evaluated to improve the heat removal in industrial carbonators for CaL TCES.

In this work, we focus on the two main gaps found in literature when assessing the utilization of calcium looping as thermochemical energy storage in concentrating solar power plants: (i) the design of a suitable reactor for carbonation at industrial scale and (ii) the analysis of the concept taken into account the reactor design and its behavior at part load operation. Thus, the novelty of this work consist in quantifying a realistic efficiency for CaL TCES at industrial scale. First, the paper introduces the concept of calcium looping TCES in CSP, establishing the case under study. Then, the methodology presents the carbonator modelling and the design criteria from few kW to

100 MW scale. Results show how part load operations in carbonator modify mass flows and the storage management (CaO, $CaCO_3$ and CO_2). Finally, we quantify the overall performance of the plant.

2. Calcium looping for energy storage in CSP plants

The energy storage system based on calcium looping process consists of two reactors, namely calciner and carbonator. In the calciner, solids fall from the top, and solar radiation provides thermal energy for calcination (Eq. (1)). In our study, we consider 100 MW of solar power input as nominal operation. If the availability of solar energy is less than the nominal power, the calciner will operate at partial load. The calciner load is defined as the ratio between the available solar power input and the nominal solar power input (100 MW). The solids mass flow is a mixture of limestone and lime (197.7 kg/s), and its inlet temperature is set at 850 ºC through the heat exchanger $HE\text{-}ER_{CaCO3+CaO}$ (Fig. 1). The operating temperature inside the calciner is kept below 950 ºC, to limit degradation of the solid particles [19].

$$CaCO_3 \leftrightarrow CaO + CO_2 \qquad \Delta H_R^0 = 180\ \mathrm{kJ/mol}, \qquad (1)$$

Lime and CO_2 are obtained after calcination of limestone. These products are conveyed to the second reactor, where carbonation takes place and the stored chemical energy is recovered (reverse of Eq. (1)). The heat released is transferred to the power block through a cooling fluid. The inlet temperature of the carbonator is set at 850 ºC [20], for which reason the heat exchangers $HE\text{-}ER_{CaO}$ and $HE\text{-}ER_{CO2}$ are used. Finally, the solids leaving the carbonator are conveyed again to the calciner, thus closing the loop.

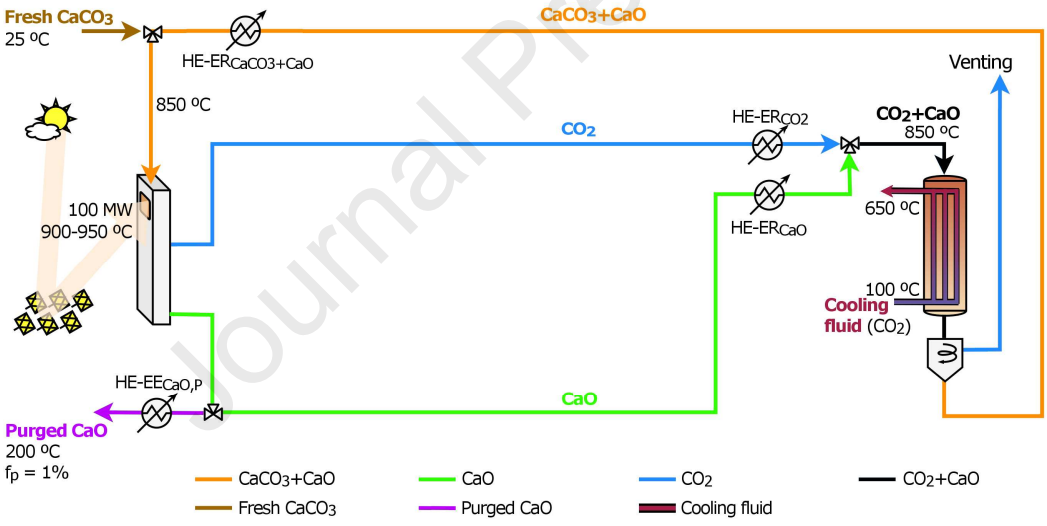

Fig. 1. Thermochemical storage system based on Ca-looping process for a large scale CSP plant: nominal operation mode.

Full calcination can be assumed at the outlet of the calciner. However, the mass composition after carbonation depends on the average sorption activity of the solid population, as only part of the CaO particle will react with the CO_2 [27]. An average maximum conversion of 13.54% is assumed for the selected limestone [26][28][29] and the molar ratio $CaO:CO_2$ at the carbonator inlet is set at 6.8:1 [28][29][30].

Additionally, a small fraction of lime is purged from the system (f_p=1%) and the corresponding amount of fresh limestone is added to compensate the removal of calcium. The addition of fresh limestone to the system increases the average sorption activity of lime population given the decay of sorption capacity of individual lime particles with the number of cycles. In this layout, lime is purged after calcination, while limestone is added at the inlet of calciner. It must be noted that there is a net input of carbon and oxygen into the system, because the carbon dioxide released from fresh limestone calcination is accumulated. Therefore, a small amount of CO_2 has to be removed from the

loop to close the carbon mass balance. Actually, the only CO_2 exiting the carbonator is this net mass input coming from the difference between the fresh $CaCO_3$ and the purged CaO, as the molar ratio in the carbonator was set to consume the rest of CO_2 during reaction.

This mode of operation corresponds to the nominal point used for carbon capture applications in which neither storage nor discharge of energy take place. The energy entering the calciner is recovered in the carbonator without delaying power production. This mode of operation is not useful for energy storage applications but its proper description is significant to understand the performance of the calcium looping. In the following subsections, the layout of the system under storage and discharge operation modes is described.

2.1. Energy storage operation mode

When the electricity demand from the system decays or the selling price of electricity does not cover the operating cost, part of the solar energy handled in the CSP is stored. Under energy storage operation, a fraction of the lime ($f_{st,CaO}$) and CO_2 ($f_{st,CO2}$) obtained through calcination are stored instead of conveyed to the carbonator (Fig. 2). Thus, the thermal power released in the carbonator is reduced, and the stored products allow producing thermal energy in a later period. Additionally, to keep constant the mass flow entering the calciner, solids must be added to the loop through the discharge from a limestone and lime reservoir. The discharge flow of this tank is defined as a fraction of the nominal solid flow leaving the carbonator outlet ($f_{dch,CaCO3}$).

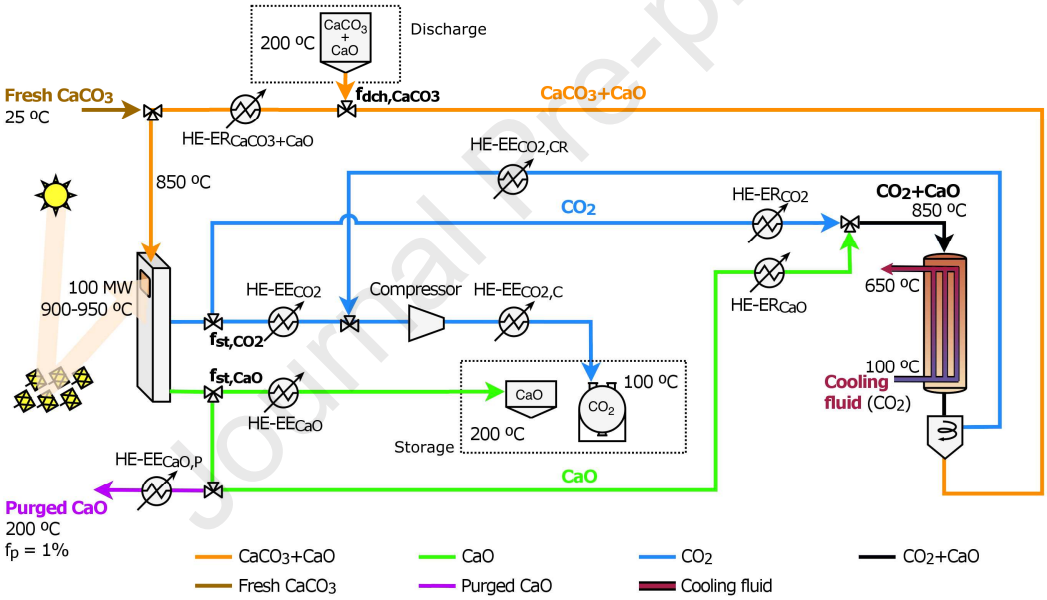

Fig. 2. Thermochemical storage system based on Ca-looping process for a large scale CSP plant: partial energy storage operation mode.

If the fraction of CaO and CO_2 sent to storage tanks increases, the load of the carbonator may be reduced below its minimum partial load, requiring to shut-down the reactor (the part load in the carbonator is defined as the ratio between the input mas flow and the nominal input mass flow). Under this situation, the plant starts operating only in storage mode, not producing thermal power in the carbonator (Fig. 3). The discharge fraction from the limestone reservoir $f_{dch,CaCO3}$ will depend on the amount of solar energy entering the receiver.

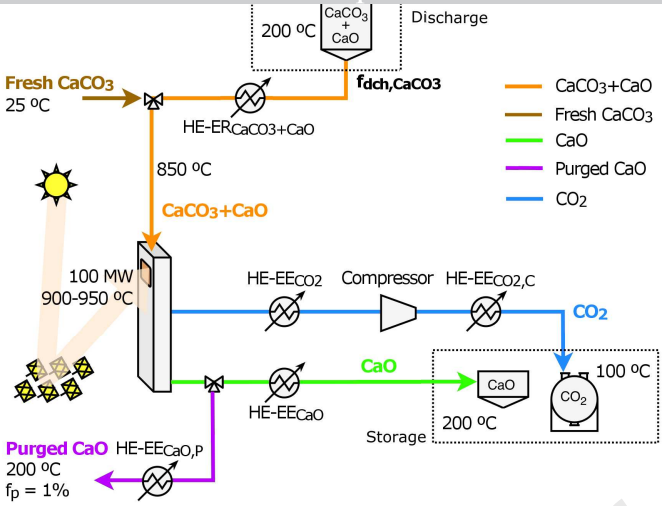

Fig. 3. Thermochemical storage system based on Ca-looping process for a large scale CSP plant: energy storage operation mode.

In this study, the properties of stored CO_2 are 100 ºC and 73 bar [20], through a compression stage including two cooling steps to 50 °C (HE-EE_{CO2}) and 100 ºC (HE-$EE_{CO2,C}$). Solids storage temperature and pressure are 200 °C (HE-EE_{CaO}) and 1 bar [19].

2.2. Energy release operation mode

Whenever solar energy is not enough to keep carbonator working at a specific load, the plant can run under energy release mode. In this case, part of the previously stored lime and CO_2 are now discharged from their reservoirs to enter in the carbonator and produce the desired thermal power (Fig. 4). The CO_2 and CaO leaving the storage tanks are defined as a fraction of the nominal flow of CO_2 ($f_{dch,CO2}$) and CaO ($f_{dch,CaO}$) at calciner outlet. Additionally, as there is not enough available solar energy to completely calcine the mass flow exiting the carbonator, part of this is diverted to storage ($f_{st,CaCO3}$) before closing the loop.

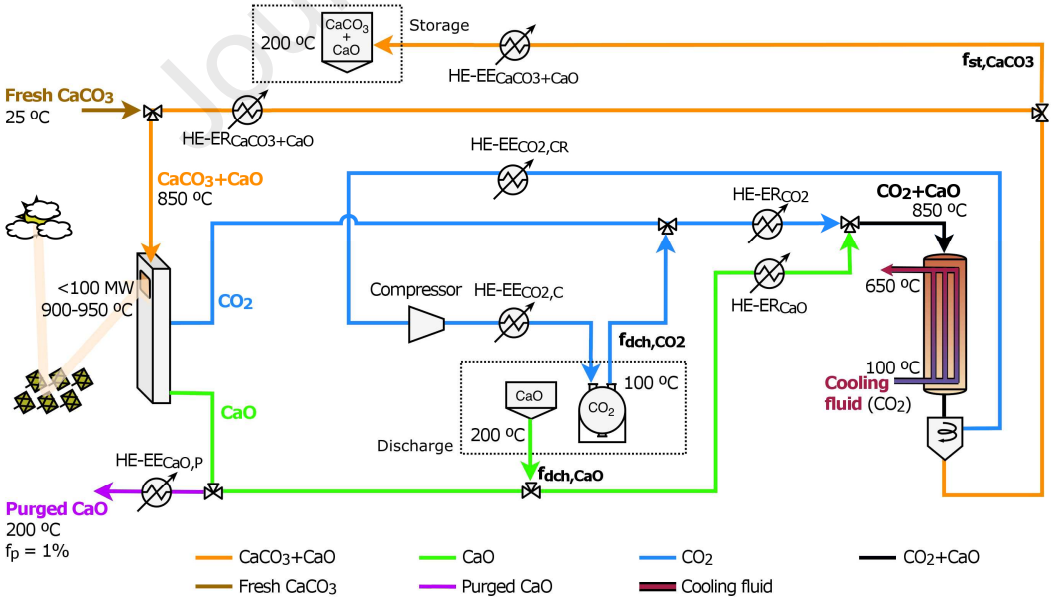

Fig. 4. Thermochemical storage system based on Ca-looping process for a large scale CSP plant: partial energy discharge operation mode.

When solar power is not available, the operation is limited to release stored energy (Fig. 5). The mass flows discharged from the reservoirs depend on the demanded thermal power to be produced. In our study, whether we store or release energy, the fractions of CaO and CO_2 entering and exiting

the tanks will be the same in order to keep constant the $CaO:CO_2$ molar ratio in the carbonator (i.e., $f_{st,CaO}=f_{st,CO2}$ and $f_{dch,CO2}=f_{dch,CaO}$). Heat losses of heat exchangers are assumed as 2% of the total released energy.

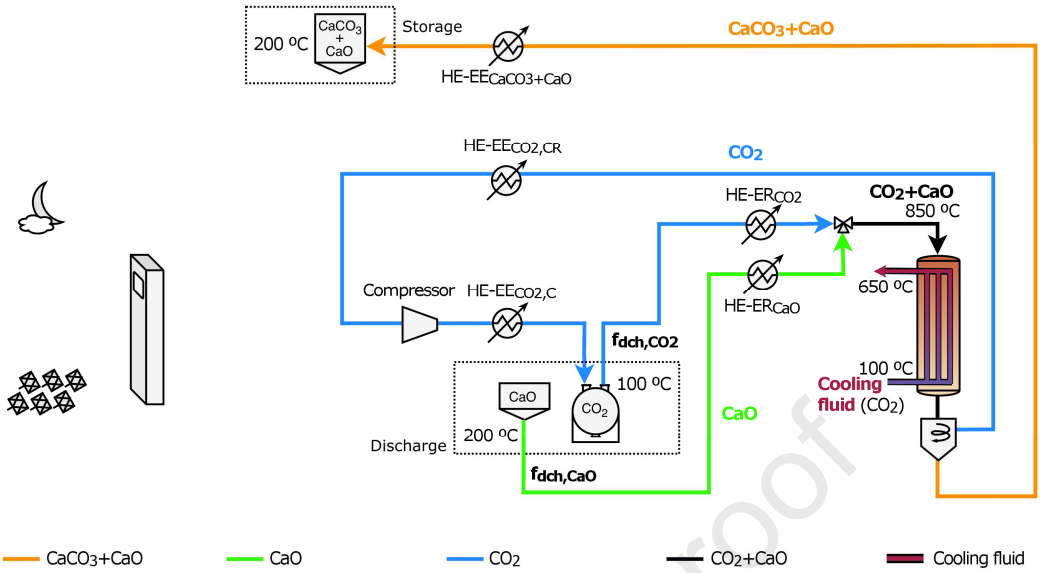

Fig. 5. Thermochemical storage system based on Ca-looping process for a large scale CSP plant: energy discharge operation mode.

3. Methodology

Methodology covers carbonator modelling, design criteria and assessment of the storage tanks required for the correct management of the plant.

3.1. Carbonator modelling

The energy removed from the carbonator represents the main source of heat sent to the power cycle. However, the operating load in the carbonator remarkably varies throughout the day due to cloud coverage, the solar radiation pattern and the demand of electricity. Therefore, its design must be assessed to quantify the effects of partial load operation in the overall efficiency of the system. In this sense, a detailed model of a large scale carbonator reactor has been developed. Besides, the minimum technical load in the carbonator have an effect on the size of storage tanks, and will determine the minimum amount of heat available for the power cycle.

The carbonator is an entrained flow reactor in which reactants entrance is located at the top. This is a complex system where heterogeneous exothermic chemical reactions take place together with heat transport phenomena. The model considers carbonation kinetics, heat transfer mechanisms and the specific geometry of the reactor, in order to compute axial profiles of conversion, temperature and residence time under different operating loads. The reactor was discretized in 100 slices of constant length, for which the equations presented in the following subsections were computed. In the case of those equations that comprise an integration, some of the variables are assumed constant along the slice to perform the integration (whenever the case, it is mentioned in the text). The model is solved in steady-state through a numerical mesh with 100 discrete 1-D elements.

The Fig. 6 illustrates the flowchart of the carbonator model for one slice of the discretized reactor. There are four main blocks that simulate the solid phase, the gas phase, the kinetics and the heat transfer. The '*gas phase*' module provides information to the '*solid phase*' module in order to compute the downward velocity of the solids falling through the reactor. Then, the '*solid phase*' module provides the residence time of the solids to the '*kinetics*' module to calculate the conversion. Also, both the '*gas phase*' and the '*solid phase*' modules transfer the mole flows data to the '*heat transfer*' module in order to calculate the final temperature inside the reactor. At this point, the computed values of conversion and temperature must be re-introduced in the different

modules (iterative process) until they converge. Once convergence is achieved, the data on residence times, conversion and temperature are provided to the next discretized slice. The former allows computing the total residence time, while conversion and temperature are used as initial values in the iterative loops of the next slice.

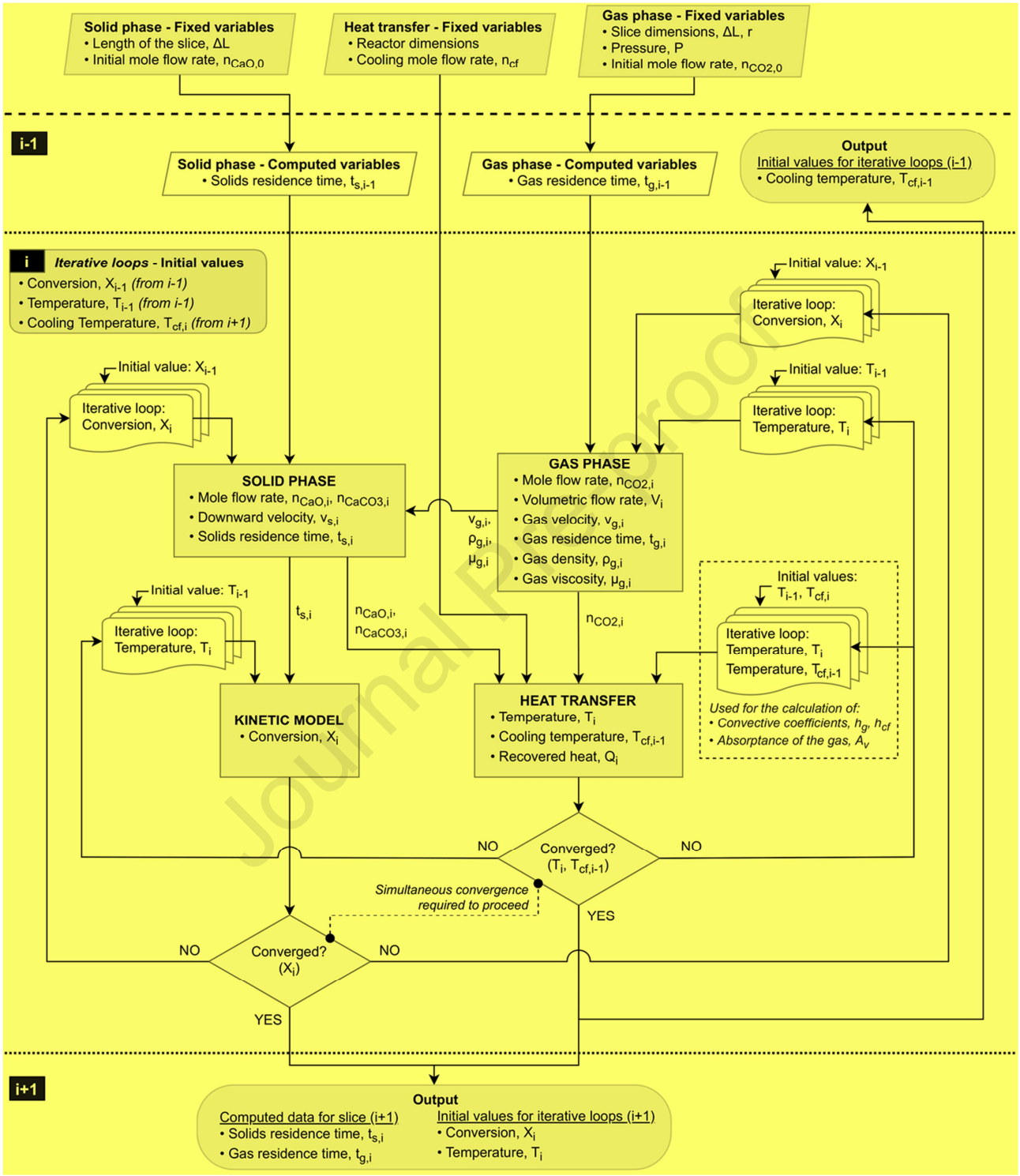

Fig. 6. Carbonator modelling flowchart for the discretized slice of index i, and its interactions with the previous (i-1) and next (i+1) slice.

It must be noted that each slice does not only depends on the previous one, but also in the following one because of the heat transfer model. Since the reactor uses a counter-current cooling configuration, the initial temperature of the cooling fluid is provided by the following slice, which is not yet solved. The boundary condition that fixed the inlet temperature of the cooling fluid, in the

last slice, allow to solve this indetermination. The final temperature of the cooling fluid is computed in the first slice. The list of boundary conditions that allow solving the system is presented in Table 1. These variables are commented in the following subsections.

Table 1. Boundary conditions of the simulation.

	$L_i = 0$	$L_i = L$	$r = r_{out,c}$
Solid phase			
mole flow rate, $\dot{n}_{CaO}$	$\dot{n}_{CaO,c,0}$ (Eq. (58))	–	–
mole flow rate, $\dot{n}_{CaCO3}$	$\dot{n}_{CaCO3,c,0} = 0$	–	–
velocity, v_s	$v_{s,0} = 0.01\ m/s$	–	–
residence time, t_s	$t_{s,0} = 0$	–	–
Gas phase			
mole flow rate, $\dot{n}_{CO2}$	$\dot{n}_{CO2,c,0}$ (Eq. (59))	–	–
velocity, v_g	$v_{g,0} = \dot{n}_{CO2,c,0} \cdot (1 - X_0) \cdot \mathcal{R} \cdot T_0 / (P \cdot S_{eff})$	–	–
residence time, t_g	$t_{g,0} = 0$	–	–
Kinetic model			
conversion, X	$X_0 = 0.00078$	–	–
Heat transfer			
Temperature of reactants, T	$T = 850\ °C$	–	–
Temperature of cooling, T_c	–	$T_c = 100\ °C$	–
Heat transferred, $\dot{q}'$	–	–	$\dot{q}' = 0$

3.1.1. Kinetic model

The kinetic equation used in the model was published by Ortiz et al [31]. The carbonation reaction is described by Eq. (2), giving the conversion of CaO as a function of time and reaction rate,

$$X(t) = \frac{X_k}{1+e^{-r(t-t_0)}}, \qquad (2)$$

where X_k is the conversion at the end of the reaction controlled phase (assumed as 0.1354 in this work) and t_0 the time taken to reach $X_k/2$ conversion (equal to 1.515 s). The reaction rate, r, is given by Eq. (3) as a function of temperature and CO_2 partial pressure,

$$r = a_2 \cdot e^{\left(-\frac{E_2}{\mathcal{R}T}\right)} \cdot \left(\frac{P}{P_{eq}} - 1\right) \cdot \left(\frac{P}{P_{eq}} + e^{(\Delta S_2^0/\mathcal{R})} e^{(-\Delta H_2^0/\mathcal{R}T_s)}\right)^{-1}, \qquad (3)$$

where E_2 is 20 kJ/mol, ΔS_2^0 is -68 J/mol·K and ΔH_2^0 is -160 kJ/mol. Besides, $P_{eq} = \mathcal{A} \cdot exp(-a/T)$, where $\mathcal{A}$ is 4.083·107 atm, and a is 20474 K.

3.1.2. Solid phase

The time spent by the solids traversing the reactor corresponds to the reaction time (i.e., the time used in Eq. (2)). This is given by the entraining downflow velocity of the solids, which depends on its terminal velocity and the gas velocity. According to Wen et al. [32], the downward velocity, v_s, of small particles under low Reynold numbers is computed by Eq. (4):

$$v_s = v_{s,i} \cdot e^{-bt_s} + \left(v_g + v_t\right) \cdot \left(1 - e^{-bt_s}\right), \qquad (4)$$

where $v_{s,i}$ is the initial velocity of the solid, v_g is the velocity of the gas phase (volumetric flow divided by the cross section), and v_t is the terminal settling velocity of the particle in a static fluid. The parameter b, and the velocity v_t are given by Eq. (5) and Eq. (6):

$$b = \frac{18\mu}{\rho_s d_p^2}, \qquad (5)$$

$$v_t = \frac{(\rho_s - \rho_g) d_p^2 g}{18\mu}, \qquad (6)$$

where μ is the viscosity of the gas, ρ_s is the density of the solid, ρ_g is the density of the gas, d_p is the diameter of the solid particles (assumed 60 micron), and g the gravity.

Integrating Eq. (4) gives the reactor length as a function of the residence time of solids, Eq. (7),

$$L = \int_0^{t_{s,L}} v_s dt_s = \frac{v_{s,i}}{b}(1 - e^{-bt_s}) + \left(v_g + v_t\right) \cdot \left(t_s - \frac{1-e^{-bt_s}}{b}\right). \qquad (7)$$

The Eq. (7) is integrated for each slice of the discretized reactor, so it can be assumed that v_g, v_t and b are constants in the range of integration (they are calculated at the specific temperature and pressure of the gas in each slice). Thus, total residence time considers the variation in temperature and gas volume along the reactor.

3.1.3. Gas phase

For the sake of simplicity, we assume that the fluid of a slice is not mixed with the fluid of any other slice ahead or behind (flat velocity profile). This implies that the residence time in the reactor is the same for all elements of the fluid. The residence time of the gas is given by Eq. (8),

$$t_g = \int_0^L \frac{S_{eff}}{\dot{V}} dL, \qquad (8)$$

where $\dot{V}$ is the volumetric flow rate and S_{eff} is the effective cross-sectional area of reactor (i.e., cross-sectional area minus the area occupied by solids). The Eq. (8) is integrated for each slice, so $\dot{V}$ and S_{eff} are constant in the interval of integration, and the residence time in that interval becomes $t_{g,\mathrm{i}} = L_i \cdot S_{eff}/\dot{V}_i$.

Besides, it is assumed that the pressure inside the reactor remains constant at 2.0 bar. The volumetric flow rate as a function of the conversion is given by Eq. (9),

$$\dot{V}_{Li} = \frac{\dot{n}_{CO2,0} \cdot (1 - X_{Li}) \cdot \mathcal{R} \cdot T_{Li}}{P} \qquad (9)$$

3.1.4. Heat transfer

In this section, it is presented (i) the energy balance on the gas-solid mixture in which carbonation takes place, (ii) the heat transference (convective and radiative) from gas-solid mixture to the walls, (iii) the conduction through walls to the cooling fluid, and (iv) the energy balance of the cooling fluid. It should be noted that heat transfer equations depend on the carbonator configuration and geometry, which have been selected differently depending on the scale (see Section 3.2). To this regard, clarifications are made when required.

3.1.4.1. Reactants side

The energy balance in the cloud of gas and particles is described by Eq. (10), considering the exothermal heat from carbonation and the heat exchange per length of reactor (from L_{i-1} to L_i):

$$\sum_j Cp_j \cdot \dot{n}_{j,L_i} \cdot \left(T_{L_i} - T_{L_{i-1}}\right) = -\Delta H_r \cdot \left(\dot{n}_{CaCO3,L_i} - \dot{n}_{CaCO3,L_{i-1}}\right) - \dot{q}'_{L_i} \cdot (L_i - L_{i-1}), \qquad (10)$$

where Cp_j and $\dot{n}_{j,}$ are the specific heat and mole flow of component j, respectively, T is the temperature of the cloud of gas and particles (assumed to be homogeneous in the slice), ΔH_r is the enthalpy of reaction (-178 kJ/mol), and $\dot{q}'_{L_i}$ is the heat flow throughout the wall per unit of axial length. This heat flow through the wall accounts for radiation, $\dot{q}'_{rad,L_i}$, and convection, $\dot{q}'_{conv,L_i}$, in the form of Eq. (11):

$$\dot{q}'_{L_i} = \dot{q}'_{rad,L_i} + \dot{q}'_{conv,L_i}, \qquad (11)$$

Radiation is given by Eq. (12):

$$\dot{q}'_{rad,L_i} = \frac{\varepsilon_w}{\alpha_{g+p} + \varepsilon_w - \alpha_{g+p} \cdot \varepsilon_w} \cdot \sigma \cdot (\varepsilon_{g+p} \cdot T_{L_i}^4 - \alpha_{g+p} \cdot T_{iw,L_i}^4) \cdot \ell\,, \qquad (12)$$

where α_{g+p} and ε_{g+p} are the absorptivity and emissivity of the gas-particle mixture [33], ε_w the emissivity of the wall, σ is the Stefan-Boltzmann constant, T is the temperature of the cloud of gas and particles (assumed to be homogeneous in the slice), and T_{iw} is the temperature of the inner wall (wall in contact with the cloud of gas and particles). The variable ℓ is defined in such a way that $\ell = \bar{a}/(L_i - L_{i-1})$, and $\bar{a}$ is the surface area where the heat transfer takes place within the slice, which depends on the geometry of the reactor.

The model for the calculation of the emissivity (ε_{g+p}) and absorptivity (α_{g+p}) of the gas-particle mixture is borne out of '*VDI Heat Atlas*', Part K4 [33]. They can be described as

$$\varepsilon_{g+p} = (1-\beta)\cdot\left(\frac{1-exp\left(-\Phi_{emi,g+p}\right)}{1+\beta\cdot exp\left(-\Phi_{emi,g+p}\right)}\right) \quad (13)$$

$$\alpha_{g+p} = (1-\beta)\cdot\left(\frac{1-exp\left(-\Phi_{abs,g+p}\right)}{1+\beta\cdot exp\left(-\Phi_{abs,g+p}\right)}\right) \quad (14)$$

with

$$\beta = \frac{\gamma-1}{\gamma+1} \quad (15)$$

$$\gamma = \sqrt{1+\frac{2\cdot\bar{Q}_{bsc}}{\bar{Q}_{abs}}} \quad (16)$$

$$\Phi_{emi,g+p} = \left(\bar{Q}_{abs}\cdot A\cdot L_p + K_{emi,g}\right)\cdot l_{mb}\cdot\gamma \quad (17)$$

$$\Phi_{abs,g+p} = \left(\bar{Q}_{abs}\cdot A\cdot L_p + K_{abs,g}\right)\cdot l_{mb}\cdot\gamma \quad (18)$$

Where $\bar{Q}_{bsc}$ and $\bar{Q}_{abs}$ are the particle scattering and absorption coefficients, $K_{emi,g}$ and $K_{abs,g}$ are the gas scattering and absorption coefficients, L_p is the particle loading, l_{mb} is the mean beam length of radiation within the relevant geometry, and A is the specific projection area of the dispersed particles.

The particle scattering and absorption coefficients ($\bar{Q}_{bsc}$ and $\bar{Q}_{abs}$) are taken from the limestone's data graph included in the Heat Atlas (reference [33], section K4, page 993) as a function of the particle diameter. The specific projection area of the dispersed particles, A, is calculated from their diameter, d_p, and density, ρ_p, by Eq. (19).

$$d_p = \frac{3}{2\cdot\rho_p\cdot A} \quad (19)$$

The gas scattering and absorption coefficients, $K_{emi,g}$ and $K_{abs,g}$, are computed from

$$K_{emi,g} = -\frac{ln\left(1-\varepsilon_g\right)}{l_{mb}} \quad (20)$$

$$K_{abs,g} = -\frac{ln(1-A_v)}{l_{mb}} \quad (21)$$

where ε_g is the emissivity of the gas and A_v is the absorptance. The values of ε_g are taken from the data graph included in the Heat Atlas (reference [33], section K3, page 982) as a function of pressure, temperature and the equivalent layer thickness. The latter is tabulated in [33], section K3, page 981, for different geometries. Regarding the absorptance A_v, it is a function of the wall temperature, the gas temperature and the emissivity of the gas, following:

$$A_v = f_{p,CO_2}\cdot\left(\frac{T_g}{T_w}\right)^{0.65}\cdot\varepsilon_g \quad (22)$$

The parameter f_{p,CO_2} is a pressure correction factor, which at 2.0 bar is equal to 1.019. This is given by equation (23), where s_{eq} is the equivalent layer thickness (tabulated in [33], section K3, page 981, for different geometries).

$$f_{p,CO_2} = 1 + (\lambda_1 - 1) \cdot exp\left[-0.5 \cdot \left(\log \frac{\lambda_2}{100 \cdot p_{CO2} \cdot s_{eq}}\right)^2\right] \quad (23)$$

with

$$\lambda_1 = \frac{\left[0.1 \cdot \left(\frac{T_g}{1000}\right)^{-1.45} + 1\right] \cdot p \cdot \left(1 + 0.28 \cdot \frac{P_{CO2}}{P}\right) + 0.23}{0.1\left(\frac{T_g}{1000}\right)^{-1.45} + p \cdot \left(1 + 0.28 \cdot \frac{P_{CO2}}{P}\right) + 0.23} \quad (24)$$

$$\lambda_2 = \begin{cases} 0.225 \cdot \left(\frac{T_g}{1000}\right)^2 & for\ T_g > 700\ K \\ 0.054 \cdot \left(\frac{T_g}{1000}\right)^2 & for\ T_g \leq 700\ K \end{cases} \quad (25)$$

Regarding convection, which is the other term of heat flow in Eq. (11), it is given by Eq. (26)

$$\dot{q}'_{conv,L_i} = h_{g,L_i} \cdot \left(T_{L_i} - T_{iw,L_i}\right) \cdot \ell, \quad (26)$$

where T is the temperature of the cloud of gas and particles (assumed to be homogeneous in the slice), T_{iw} is the temperature of the inner wall (wall in contact with the cloud of gas and particles) and h_g the convective coefficient [34]. The variable ℓ is defined in such a way that $\ell = \bar{a}/(L_i - L_{i-1})$, and $\bar{a}$ is the surface area where the heat transfer takes place within the slice, which depends on the geometry of the reactor.

The convective coefficient at each axial position is calculated by Eq. (27) [34]:

$$h_{g,L_i} = \frac{Nu_{Li} \cdot k_{Li}}{D_h} \quad (27)$$

Where Nu is the Nusselt number, k the thermal conductivity of the gas (at T_{L_i} and P_{L_i}) , and D_h the hydraulic diameter. The latter is defined according to Eq. (28), which relates the cross-sectional area of the flow, S_{eff}, and the perimeter of the section, per.

$$D_h = \frac{4 \cdot S_{eff}}{per} \quad (28)$$

It should be noted that the hydraulic diameter depends on the geometry of the reactor. In our study, we use two types of configuration (see Fig. 7): an annular single-tube (reactants in the outer side) and a tube bundle in triangle configuration (reactants in the shell side). The hydraulic diameter for these two cases are:

$$D_{h(annular)} = 2 \cdot (r_c - r_{cf}) \quad (29)$$

$$D_{h(bundle)} = \frac{2 \cdot \left(r_c^2 - N \cdot r_{cf}^2\right)}{\left(r_c + N \cdot r_{cf}\right)} \quad (30)$$

Where r_c is the radius of the carbonator tube (the enclosing), r_{cf} is the radius of the cooling tube, and N the number of cooling tubes.

The Nusselt number, which is necessary in Eq. (27), also depends on the geometry of the reactor. In the case of an annular configuration, the correlations developed by Bennett are used [35]. Specifically, the correlation corresponding to boundary conditions of adiabatic outer wall and constant inner wall temperature (in our simulation, we use the average temperature of the cooling wall for the calculation of the Nusselt number). The Nusselt number in the inner surface, at an axial position L_i (of the total length L) is given by Eq. (31):

$$Nu_{Li(annular)} = \overline{Nu}_{L(annular)} \cdot \left(1 - \frac{\left(\frac{Gz_{Li}}{3}\right) \Big/ \left(Gz_{Li}^{n/3} + \left(\frac{Nu_\infty - O_{Lev}}{A \cdot (fRe_D)^{1/3}}\right)^n \right)}{1 + \left(\frac{O_{Lev}}{A \cdot (fRe_D)^{1/3}}\right) \Big/ \left(Gz_{Li}^{n/3} + \left(\frac{Nu_\infty - O_{Lev}}{A \cdot (fRe_D)^{1/3}}\right)^n \right)^{1/n}} \right) \quad (31)$$

Where $\overline{Nu}_{L(annular)}$ is the average Nusselt number over the total axial length of the reactor, fRe_D is the friction factor, Nu_∞ is the Nusselt number for fully developed heat transfer, O_{Lev} is the offset in the extended Lévêque solution, n is an exponent factor, A is a constant factor equal to 0.40377, and Gz_{Li} is the Graetz number for a duct of length L_i. These variables are computed by Eq. (32) to (37).

$$\overline{Nu}_{L(annular)} = \left[\left(A \cdot (fRe_D \cdot Gz_{Li=L})^{1/3} \right)^n + (Nu_\infty - O_{Lev})^n \right]^{1/n} + O_{Lev} \quad (32)$$

$$fRe_D = 32 \cdot \left(\frac{1 - r_*}{r_*}\right) \cdot \left(\frac{-2 \cdot r_*^2 - (1 - r_*^2)/\ln(r_*)}{1 + r_*^2 + (1 - r_*^2)/\ln(r_*)} \right) \quad (33)$$

$$Nu_\infty = 4.224 - 1.492 \cdot r_*^{-1/3} + 1.972 \cdot r_*^{-2/3} + 0.1370 \cdot r_*^{-1} \quad (34)$$

$$O_{Lev} = Nu_\infty^2/310 + 0.911 \cdot Nu_\infty - 4.81 \qquad (4 < Nu_\infty < 24) \quad (35)$$

$$n = A^3 \cdot exp(fRe_D/350 + 3.6) \qquad (70 < fRe_D < 400) \quad (36)$$

$$Gz_{Li} = D_h \cdot Re_{D,Li} \cdot Pr_{Li}/L_i \quad (37)$$

Where A is the same constant factor than before (equal to 0.40377), r_* is the ratio between the inner and outer radius (i.e., between de radius of the cooling tube and the carbonator tube, Eq. (38)), $Re_{D,Li}$ is the Reynolds number based on the hydraulic diameter at the axial position L_i (Eq.(39)), and Pr is the Prandtl number at the axial position L_i (Eq.(40)):

$$r_* = r_{cf}/r_c \qquad (1/50 \leq r_* < 1) \quad (38)$$

$$Re_{D,Li} = \frac{\dot{m}_{Li} \cdot D_h}{S_{eff} \cdot \mu_{Li}} \quad (39)$$

$$Pr_{Li} = Cp_{Li} \cdot \mu_{Li}/k_{Li} \quad (40)$$

Alternatively, in the case of a tube bundle configuration with longitudinal flow, the Nusselt number is calculated through the correlations of Taborek [36]. Taborek only provided the correlations for the average Nusselt number over the total length of the reactor, instead of the local Nusselt number at position L_i. The correlation for the laminar region follows Eq. (41), which will be the case of our reactor (correlations for the transition and turbulent flow can be seen in reference [36]):

$$\overline{Nu}_{L(bundle)} = \left[Nu_\infty^3 + 9.261 \cdot Re_{D,L} \cdot Pr_L \cdot D_h/L \right]^{1/3} \qquad (Re_D < 500) \quad (41)$$

Where Nu_∞ is equal to 4.12 (in this case, it represents the solution as Re tends to 0), $Re_{D,L}$ is the Reynolds number calculated as Eq. (39) with the corresponding $D_{h(bundle)}$ of Eq. (30), Pr_L is the Prandtl number as Eq. (40), D_h is the hydraulic diameter for tube bundle (Eq. (30)) and L is the total length of the reactor.

In order to compute the local Nusselt number for the tube bundle configuration, the correlation of Taborek can be differentiated according to Eq. (42) [37] (note that this expression is only valid for ducts of constant wall temperature):

$$Nu_{Li} = \frac{d}{dL}(\overline{Nu}_L \cdot L)\Big|_{L=L_i} \quad (42)$$

Thus, the local Nusselt number in a tube bundle (shell side) can be computed through Eq. (43) as:

$$Nu_{Li(bundle)} = \frac{Nu_\infty^3 + 6.174 \cdot Gz_{Li}}{(Nu_\infty^3 + 9.261 \cdot Gz_{Li})^{2/3}} \qquad (Re_D < 500) \quad (43)$$

Where Nu_∞ is equal to 4.12 and the Graetz number is calculated with Eq. (37) using the corresponding $D_{h(bundle)}$ of Eq. (30).

3.1.4.2. Cooling side

The heat conducted through the wall separating the cooling and reactants is given by Eq. (44), which allows computing the temperature of the wall side that is in contact with the cooling fluid, T_{ow}:

$$\frac{\dot{q}'_{L_i}}{N} = \frac{T_{iw,L_i} - T_{ow,L_i}}{R_{tube} \cdot L_i} \quad (44)$$

$$R_{tube} = \frac{ln(\frac{r_{out}}{r})}{2\pi \cdot k_{tube} \cdot L_i} \quad (45)$$

where R_{tube} is the thermal resistance of the cooling tube, r_{out} and r the outer and inner radius of the cooling pipe, N the number of cooling tubes, and k_{tube} the thermal conductivity of the tube (0.025 kW/m·K).

Once the temperature of the inner wall of the cooling tube is known, the energy balance on the cooling fluid is performed, by Eq. (46):

$$Cp_{cf} \cdot \dot{n}_{cf} \cdot \left(T_{cf,L_i-1} - T_{cf,L_i}\right) = \dot{q}'_{L_i} \cdot (L_i - L_{i-1}), \quad (46)$$

where Cp_{cf} and $\dot{n}_{cf}$ are the specific heat and mole flow of the cooling fluid. It should be noted that Eq. (46) is valid for a countercurrent heat exchange, and therefore it is heated from position L_i to L_{i-1} (carbonation goes from position L_{i-1} to L_i).

The heat transferred to the cooling fluid per unit of axial length, Eq. (47), is composed by the convective and radiative terms:

$$\dot{q}'_{L_i} = \dot{q}'_{rad,cf,L_{i-1}} + \dot{q}'_{conv,cf,L_{i-1}}, \quad (47)$$

Radiation is given by Eq. (48):

$$\dot{q}'_{rad,cf,L_{i-1}} = \frac{\varepsilon_w}{1-(1-\varepsilon_w)(1-A_{v_{cf,L_i}})} \cdot \sigma \cdot (A_{v_{cf,L_i}} \cdot T^4_{\mathrm{ow},L_i} - \varepsilon_{cf} \cdot T^4_{cf,L_i}) \cdot \ell_{\mathrm{cf}}, \quad (48)$$

where $A_{v,cf}$ is the geometry-dependent absorptance of the cooling fluid (calculated through Eq. (22), since we assume CO_2 as cooling fluid), ε_w the emissivity of the wall, σ is the Stefan-Boltzmann constant, T_{ow} is the temperature of the wall in contact with the cooling fluid, and T_{cf} is the temperature of the cooling fluid. The variable ℓ is defined in such a way that $\ell = \bar{a}/(L_i - L_{i-1})$, and $\bar{a}$ is the surface area where the heat transfer takes place within the slice.

Regarding convection, which is the other term of heat flow in Eq. (47), it is given by Eq. (49)

$$\dot{q}'_{conv,cf,L_{i-1}} = h_{cf,L_{i-1}} \cdot \left(T_{ow,L_i} - T_{cf,L_{i-1}}\right) \cdot \ell_{\mathrm{cf}}, \quad (49)$$

where h_{cf} is the convective coefficient of the cooling fluid, , T_{ow} is the temperature of the wall in contact with the cooling fluid, and T_{cf} is the temperature of the cooling fluid. The variable ℓ is defined in such a way that $\ell = \bar{a}/(L_i - L_{i-1})$, and $\bar{a}$ is the surface area where the heat transfer takes place within the slice, which depends on the geometry of the reactor.

The convective coefficient at each axial position is calculated by Eq. (27), with the corresponding D_h computed with Eq. (28). In the cooling side, we have a circular tube configuration, so the hydraulic diameter is the one presented in Eq. (50):

$$D_{h(tube)} = 2 \cdot r_{cf} \quad (50)$$

The Nusselt number for this configuration is calculated through the correlation of Nellis G and Klein S (Eq. (51)) [34]. This expression provides the average Nusselt number over the length of the cooling tube, assuming constant temperature wall:

$$\overline{Nu}_{L(tube)} = 3.66 + \frac{(0.049 + 0.020/Pr_L) \cdot Gz_L}{1 + 0.065 \cdot Gz_L^{0.7}} \quad (51)$$

To compute the local Nusselt number at an axial position L_i, Eq. (42) is used, obtaining the following expression (Eq. (52)):

$$Nu_{Li(tube)} = 3.66 + \frac{Gz_{Li}^{1.12} \cdot (1.8473 \cdot Gz_{Li}^{0.7} \cdot Pr_{Li} + 0.754 \cdot Gz_{Li}^{0.7} - 5.88 \cdot Pr_{Li} - 2.4)}{10^3 \cdot Pr_{Li} \cdot \left(1 + 0.065 \cdot Gz_{Li}^{0.7}\right)^2} \quad (52)$$

Where the Graetz and Prandtl numbers are calculated with Eq. (37) and Eq. (40).

With this methodology, the temperature along the carbonator can be calculated by knowing the initial temperature of reactants and cooling fluid.

3.2. Design criteria at different scales

The scale of the system is characterized by the solar power available in the calciner, $\dot{Q}_{CL}$ (from 10 kW to 100 MW). The corresponding input flows of CaO and CO_2 entering the carbonator (at nominal load) are computed through the energy balance in the calciner (Eq. (53)).

$$\dot{Q}_{CL} = \mathrm{h}_{CaO}^{(950°C)} \cdot \dot{n}_{CaO,c,0} + \mathrm{h}_{CO2}^{(950°C)} \cdot \dot{n}_{CO2,c,0} + \mathrm{h}_{CaO}^{(950°C)} \cdot \dot{n}_{CaO,p} - \mathrm{h}_{CaCO3}^{(850°C)} \cdot \dot{n}_{CaCO3,c,out} - \mathrm{h}_{CaO}^{(850°C)} \cdot \dot{n}_{CaO,c,out} - \mathrm{h}_{CaCO3}^{(25°C)} \cdot \dot{n}_{CaCO3,f} \quad (53)$$

where h_j^T is the specific enthalpy of the component j at temperature T, $\dot{n}_{j,c,0}$ is the mole flow of component j entering the carbonator (which are outlet flows in the calciner), $\dot{n}_{j,c,out}$ is the mole flow of component j exiting the carbonator (which are inlet flows in the calciner), $\dot{n}_{CaO,p}$ is the lime purged after exiting the calciner, and $\dot{n}_{CaCO3,f}$ is the fresh limestone introduced in the calciner to replace the purge. All these mole flows can be written as a function of $\dot{n}_{CaO,c,0}$ (Eq. (54) to Eq. (57)) by fixing the conversion achieved in the carbonator (assumed as X_K=0.1354) and the CaO:CO_2 molar ratio (R = 6.8776).

$$\dot{n}_{CO2,c,0} = \frac{\dot{n}_{CaO,c,0}}{\mathrm{R}} \quad (54)$$

$$\dot{n}_{CaCO3,c,out} = \dot{n}_{CaO,c,0} \cdot X_K \quad (55)$$

$$\dot{n}_{CaO,c,out} = \dot{n}_{CaO,c,0} \cdot (1 - X_K) \quad (56)$$

$$\dot{n}_{CaO,p} = \dot{n}_{CaCO3,f} = \dot{n}_{CaO,c,0} \cdot \left(\frac{1}{\mathrm{R}} - X_K\right) \quad (57)$$

Operating in Eq. (53) and using enthalpy data from Aspen Plus database, it is found Eq. (58) and Eq. (59) for the calculation of the nominal input flows of CaO and CO_2 in the carbonator as a function of the solar power entering the calciner.

$$\dot{n}_{CaO,c,0} = \frac{\dot{Q}_{CL}}{32{,}162.19\ \left[\frac{kJ}{kmol}\right]} \quad or \quad \dot{m}_{CaO,c,0} = \frac{\dot{Q}_{CL}}{573.53\left[\frac{kJ}{kg}\right]} \quad (58)$$

$$\dot{n}_{CO2,c,0} = \frac{\dot{Q}_{CL}}{221{,}198.68\ \left[\frac{kJ}{kmol}\right]} \quad or \quad \dot{m}_{CO2,c,0} = \frac{\dot{Q}_{CL}}{5{,}027.24\left[\frac{kJ}{kg}\right]} \quad (59)$$

In addition to the input flow calculation, some design criteria have been followed to keep similar conversion and temperature profiles along the reactor at different scales. First, a single tube reactor with inner cooling has been modelled, looking for proper heat removal at small scale (10 kW). This reactor is made of two concentric tubes of small diameter. The reactants flow from top to bottom through the outer tube, while cooling fluid flows in counter-current throughout the inner tube (Fig. 7). The aim is to recover few kW at this stage. The required input flows for 10 kW are 0.0174 kg/s of CaO and 0.0020 kg/s of CO_2.

Once proper dimensions are fixed for single-tube, a multi-tube configuration is stablished. This multi-tube reactor encloses 150 – 200 cooling tubes, between which the reactants flow from top to

bottom. In principle, the cooling pipes are of the same diameter and length that the one used in single-tube configuration (the enclosure is also of the same length than the cooling pipes). The cooling tubes are set in triangular configuration and the distance among them is fixed in order to keep the cross-sectional area in proportion to the increment of reactants volume. In other words, the cross-sectional area through which the reactants flow is N times the area of the single tube configuration, being N the number of cooling tubes inside the enclosure of the multi-tube. This configuration is aimed to reach the MW scale (about $\dot{Q}_{CL} = 2$ MW), by keeping similar temperature profiles along the reactor.

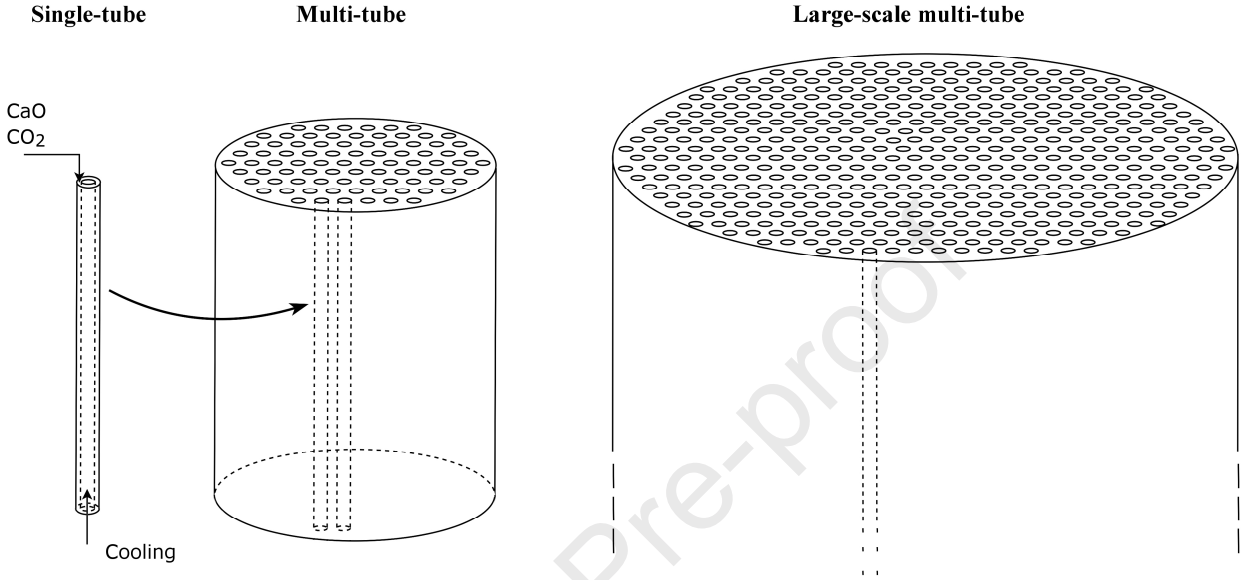

Fig. 7. Carbonator configurations for small and large scale.

Lastly, the large-scale multi-tube configuration is designed by keeping constant the ratio between the length of the reactor and the velocity of the gas-solid mixture flowing downward (L/v), and the ratio between the length of the reactor and the diameter of the enclosure (L/d) [38]. Besides, the number of cooling tubes is increased, instead of increasing their diameter. The aims of this configuration is to achieve the 100 MWth scale and to quantify the behavior at partial load. Again, we look for conserving temperature profiles, and outlet temperatures of both products and cooling fluids, since power production is the main objective of this reactor.

3.3. Operation modes and efficiency definitions

The two operations considered in this study are energy storage operation mode (ESOM) and energy release operation mode (EROM). Under these modes, a large number of operation points leads to different pairs of calciner-carbonator powers and different values of storage power. The operation points are related to the mass flowrates stored or released from the tanks.

3.3.1. Energy storage operation mode

Two parameters are used to describe the operation points of ESOM: the fraction of the lime produced in the calciner that is sent to storage, and the fraction of limestone in the tank that is discharged.

The storage fraction of lime, $f_{st,CaO}$ in Eq. (60), is the ratio between the mass flowrate diverted to the CaO storage tank and the maximum mass flowrate that could leave the calciner operating at full capacity (100 MW).

$$f_{st,CaO} = \frac{\dot{m}_{CaO,st}}{\dot{m}_{CaO,max}} \qquad (60)$$

The discharge fraction of limestone, $f_{dch,CaCO3}$ in Eq. (61), is the ratio between the mass flowrate discharged from the limestone tank and the maximum mass flowrate that could leave the carbonator operating at full capacity.

$$f_{dch,CaCO3} = \frac{\dot{m}_{CaCO3+CaO,dch}}{\dot{m}_{CaCO3+CaO,max}} \qquad (61)$$

All the potential pairs of these two parameters cover the operation points encompassed during ESOM.

The specific storage consumption (*SSC*) expressed in Eq. (62) provides the amount of total energy (thermal and electrical) required to store a mass unit of lime. This value is useful to understand whether the storage process is profitable or not in terms of energy under specific operation points. It must be kept in mind the qualitative interest of the parameter but its limitation as quantitative measure given the mix of energy types in its definition. The energy consumed in the process includes the fraction of heat used to produce the lime sent to the storage tank ($\dot{Q}_{CL,st}$), the preheating of the limestone discharged from the storage tank which is later stored in the form of lime ($\dot{Q}_{HE\ ER\ CaCO3,st}$) and the electric power demanded in the compression of the stored carbon dioxide ($\dot{W}_{compressor}$).

$$SSC = \frac{\dot{Q}_{CL,st}+\dot{Q}_{HE\ ER\ CaCO3,st}+\dot{W}_{compressor}}{\dot{m}_{CaO,st}} \qquad (62)$$

A storage efficiency, η_{st}, is defined by Eq. (63) to compare the amount of stored energy and the net energy consumed during the storage process. The stored energy comprises the sensible heat of the stored substances (lime and carbon dioxide, $CS_{CO2+CaO,st}$) and the chemical energy potentially stored in the lime which will be latter carbonated, $\Delta H_R^0 \cdot \dot{n}_{CaCO3,CR}$. This parameter provides an idea of the portion of energy that is stored and the portion that is lost during the storage process.

$$\eta_{st} = \frac{\dot{Q}_{st,CaO}}{\dot{Q}_{CL,st}+\dot{Q}_{HE\ ER\ CaCO3,st}+\dot{W}_{compressor}} = \frac{CS_{CO2+CaO,st}+\Delta H_R^0 \cdot \dot{n}_{CaCO3,CR}}{\dot{Q}_{CL,st}+\dot{Q}_{HE\ ER\ CaCO3,st}+\dot{W}_{compressor}} \qquad (63)$$

Another significant value for the operation is the efficiency of the carbonator in reference to the energy provided by this equipment, η_{CR}, Eq. (64). It compares the amount of power released in the carbonator and the energy invested. The latter includes the heat of calcination required to produce the lime fed into the carbonator, $\dot{Q}_{CL,CR}$, and the preheat of this limestone prior the calciner, $\dot{Q}_{HE\ ER\ CaCO3,CR}$.

$$\eta_{CR} = \frac{\dot{Q}_{CR}}{\dot{Q}_{CL,CR}+\dot{Q}_{HE\ ER\ CaCO3,CR}} \qquad (64)$$

Finally, an efficiency related to the available thermal energy is defined by Eq. (25) and Eq. (65), with the former including the sensible heat of the stored substances. This efficiency compares the available heat to the energy invested. The available heat accounts for the thermal power released in the carbonator, and the thermal power provided by the different heat exchangers (EE heat exchangers always provide thermal power, while ER heat exchangers only provide thermal power under ESOM).

$$\eta_{av,1} = \frac{\dot{Q}_{CR}+\sum \dot{Q}_{HE\ EE}+\dot{Q}_{HE\ ER\ CO2}+\dot{Q}_{HE\ ER\ CaO}}{\dot{Q}_{CL}+\dot{Q}_{HE\ ER\ CaCO3}+CS_{CaCO3+CaO,dch}} \qquad (25)$$

$$\eta_{av(ESOM)} = \frac{\dot{Q}_{CR}+\sum \dot{Q}_{HE\ EE}+\dot{Q}_{HE\ ER\ CO2}+\dot{Q}_{HE\ ER\ CaO}}{\dot{Q}_{CL}+\dot{Q}_{HE\ ER\ CaCO3}} \qquad (65)$$

3.3.2. Energy release operation mode

Analogously, the storage fraction of the limestone produced in the carbonator, Eq. (66), and the discharge fraction of lime from the storage tanks, Eq. (67), describe the set of operation points that conform the energy release operation mode.

$$f_{st,CaCO3} = \frac{\dot{m}_{CaCO3+CaO,st}}{\dot{m}_{CaCO3+CaO,max}} \quad (66)$$

$$f_{dch,CaO} = \frac{\dot{m}_{CaO,dch}}{\dot{m}_{CaO,max}} \quad (67)$$

The storage fraction of limestone, $f_{st,CaCO3}$, represents the ratio between the mass flowrate diverted to the storage tank from the outlet stream of the carbonator and the maximum mass flowrate which could leave the carbonator operating at full capacity. The discharge fraction of lime, $f_{dch,CaO}$, is the relation between the mass flowrate discharged from the CaO tank and the maximum mass flowrate of CaO leaving the calciner at full load.

The energy efficiency in the carbonator, η_{CR}, under EROM is calculated through Eq. (68). The energy invested in this process includes (i) all the heat of calcination demanded in the calciner, $\dot{Q}_{CL}$, (since no calcined material is diverted to storage tanks under EROM) (ii) the storage consumption of the mass flowrate of lime discharged from the tanks, (iii) the preheating of this limestone before introduced into the calciner, $\dot{Q}_{HE\ ER\ CaCO3}$ and (iv) the preheating of the mass flowrates of lime and carbon dioxide, $\dot{Q}_{HE\ ER\ CO2}$ and $\dot{Q}_{HE\ ER\ CaO}$ (if needed).

$$\eta_{CR} = \frac{\dot{Q}_{CR}}{\dot{Q}_{CL}+SSC\cdot\dot{m}_{CaO,dch}+\dot{Q}_{HE\ ER\ CaCO3}+\dot{Q}_{HE\ ER\ CO2}+\dot{Q}_{HE\ ER\ CaO}} \quad (68)$$

Under EROM, the thermal efficiency of the system is defined both considering, Eq. (30), and not considering, by Eq. (69), the sensible heat of the stored substances. In this case, the available heat only includes the thermal power from the carbonator and EE heat exchangers.

$$\eta_{av,1} = \frac{\dot{Q}_{CR}+\sum \dot{Q}_{HE\ EE}}{\dot{Q}_{CL}+\dot{Q}_{HE\ ER\ CaCO3}+CS_{CaO,dch}+CS_{CO2,dch}+SSC\cdot\dot{m}_{CaO,dch}+\dot{Q}_{HE\ ER\ CO2}+\dot{Q}_{HE\ ER\ CaO}} \quad (30)$$

$$\eta_{av(EROM)} = \frac{\dot{Q}_{CR}+\sum \dot{Q}_{HE\ EE}}{\dot{Q}_{CL}+\dot{Q}_{HE\ ER\ CaCO3}+SSC\cdot\dot{m}_{CaO,dch}+\dot{Q}_{HE\ ER\ CO2}+\dot{Q}_{HE\ ER\ CaO}} \quad (69)$$

3.4. Sizing of storage tanks

The sizing of storage tanks accounts for the operating mode and the introduced/extracted mass flowrates of CO_2, CaO and $CaCO_3$. The operating mode dictates the number of hours and the storage/discharge fractions. Storage and discharge fractions directly define the inlet and outlet flowrates, while the number of hours provides the time interval to integrate. The storage volume of the tanks is calculated through Eq. (70).

$$V_{st}(t) = \int_{t_0}^{t} \left(\frac{\dot{m}_{in}-\dot{m}_{out}}{\rho}\right) dt + V_{st,0} \quad (70)$$

The maximum storage flowrate of CO_2 and CaO takes place when solar calciner operates at nominal load and carbonator operates at minimum load.

4. Results

In this section, the model validation and the results for the small- and large-scale carbonators are presented. Besides, it is assessed the partial load operation for the large-scale carbonator. Lastly, a model of the coupled CaL TCES and CSP systems is run at threshold operation conditions to provide the sizing of storage tanks.

4.1. Model validation

The first important issue to be validated is the independency of results with respect to the number of discretized elements (i.e., with the length of each discretized slice). As case of study, it has been

chosen the single-tube configuration operating at 50% partial load (the part load in the carbonator is defined as the ratio between the input mass flow and the nominal input mass flow). The Fig. 8 presents the relative error that exists in the most important computed variables versus the number of discretization elements, with respect to 300 discretization elements (in a 4-meter reactor, the latter means slices of 1.3 cm). It can be seen that the relative error remains below 1% in all cases whenever the number of discretization elements is above 15. Therefore, we select 100 discretization elements for the simulations presented in Section 4.2.

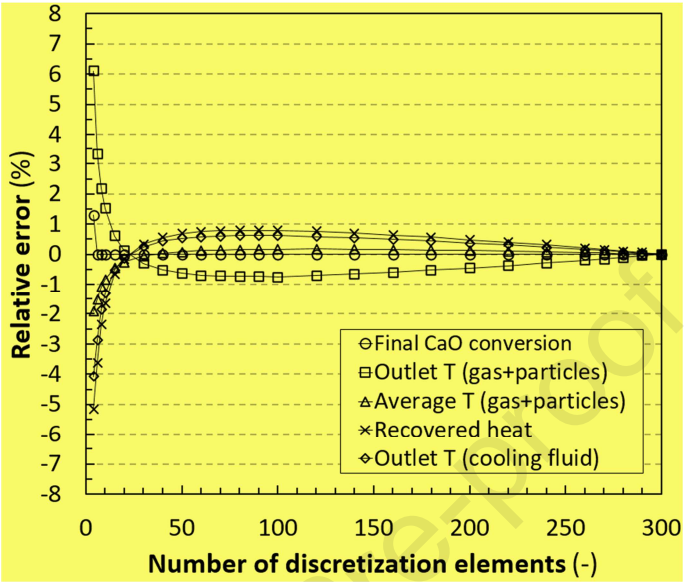

Fig. 8. Relative error in the most relevant computed variables vs. the number of discretization elements (with respect to 300 discretization elements).

These small variations in the computed variables come from assuming constant volume flow in Eq. (8) when integrating over the length of each discretized element. This can be clearly seen in Fig. 9 when comparing the temperature and conversion profiles of a simulation with 100 discretization elements (depicted with symbols) with a simulation with 300 discretization elements (depicted with lines). In those regions in which the variation of volume flow occurs faster (i.e., with higher reaction rates), the error becomes noticeable. It must be noted that, since the case chosen as example is operating at 50% partial load, the reaction occurs in a shorter length, what accentuates the relative error. If the reactor operates at full load, the variation in volume is less steep, and the error less significant.

Furthermore, the selected operating conditions in our simulations make CO_2 to react almost completely, so any variation in volume flow is remarkable compared to the total volume flow in the reactor. This makes the relative error to be more significant. Still, our simulation keeps relative errors below 1% in the variables of interest. In the case of analysing a reactor setup with higher ratio of CO_2:CaO, the error would be even lower.

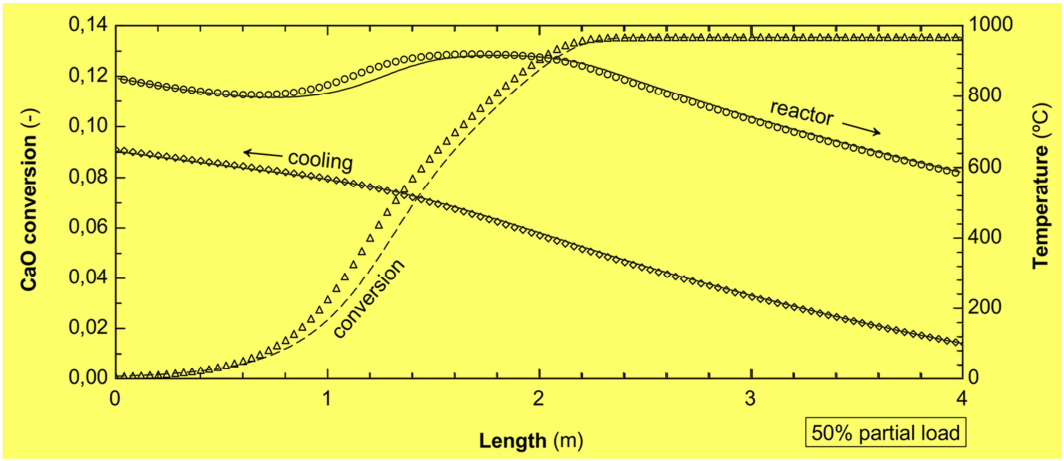

Fig. 9. Comparison between 100 (symbols) and 300 (lines) discretization elements, for the results on CaO conversion and temperature profiles (reactor and cooling sides) vs. length (from top to bottom), in a single-tube carbonator operating at 50% partial load.

The second important issue to be validated is the reproducibility of experimental results. In this aspect, the model is validated using experimental results of an entrained flow carbonator from Plou et al. [39]. The reactor of Plou et al. is a 24-meter spiral-shaped stainless steel tube, with an external diameter of 3/8" (inner diameter of 7.54 mm). The gas velocity used during the experiments avoids saltation conditions within the entrained flow regime (i.e., avoids falling of particles towards the wall). The reactor is kept isothermal at 650 °C along the whole path. Three different materials were analysed: two types of high-purity calcined lime and one cement raw meal. The results of the material tagged as "Lime #1" are used in this study for comparison as it has a similar value of X_k (i.e., conversion at the end of the reaction controlled phase) and t_0 (i.e., the time taken to reach a $X_k/2$ conversion) than the material assumed in the simulations of this study. Lime #1 has $X_k = 0.10$ and t_0 about 2 seconds, while the material used in our simulations has $X_k = 0.1354$ and $t_0 = 1.515$ seconds. These are typical conversions of highly deactivated materials.

The Fig. 10 shows the CO_2 capture efficiency, which is defined as the CO_2 captured versus the maximum possible according to the equilibrium. The experiments were carried out with a gas velocity of 13.5 m/s at 650 °C and 1 bar (about $2.4 \cdot 10^{-4}$ kg/s). The gas is composed of 10% CO_2 and 90% air. The mass ratio between the solid and the gas was varied between 0.125 and 0.400 by modifying the mass of CaO entered in the reactor.

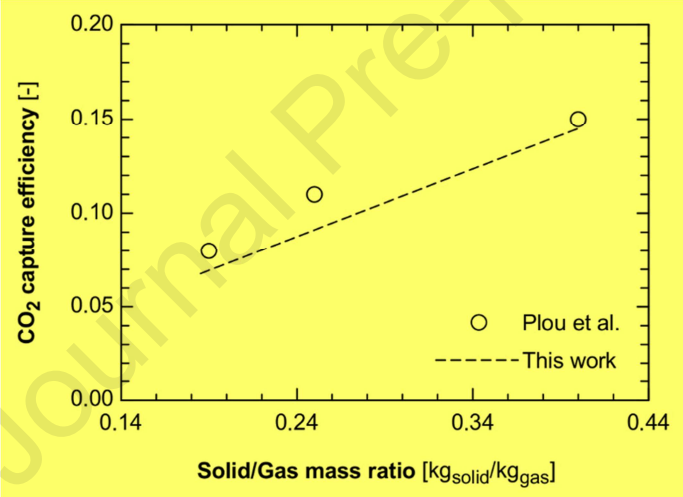

Fig. 10. CO_2 capture efficiency achieved in the entrained flow reactor of Plou et al. [39] *and in the simulations of this study under the same setup, as a function of the solid/gas mass ratio.*

The results show a good agreement with the experiments of Plou et al. for Lime #1. The measured residence time is 1.8 seconds, while the simulated residence time 1.78 seconds for the gas and 1.77 seconds for the solids.

4.2. Carbonator assessment

The technical data regarding the three carbonators under study are presented in Table 2 (single-tube at lab scale, 7.6 kW, multi-tube at pilot scale, 1.4 MW, and the large-scale multi-tube, 79.9 MW). The reactants enter at 850 ºC and 2 bar, and the cooling fluid is CO_2 entering at 100 ºC and 50 bar. The mass of the cooling fluid is calculated to set its exit temperature at 650 ºC.

Table 2. Technical data of the studied carbonators.

	Single-tube	*Multi-tube*	*Large-scale multi-tube*	
Carbonator				
Length (m)	4.0	5.0	15.0	Design criteria (Section 3.2)
Enclosure inner diameter (m)	0.074	0.970	3.3	Design criteria (Section 3.2)
CaO mass inlet (kg/s)	0.01740	3.2533	178.6	Eq. (58)

CO_2 mass inlet (kg/s)	0.00198	0.3712	20.8	Eq. (35)
Final CaO conversion (%)	13.53	13.54	13.54	Output of the model
Gas residence time (s)	7.1	10.0	7.55	Output of the model
Solid residence time (s)	4.8	6.6	6.51	Output of the model
Inlet T (ºC)	850.0	850.0	850.0	Boundary condition
Outlet T (ºC)	850.7	844.8	841.1	Output of the model
Average T (ºC)	850.8	871.5	850.6	Output of the model
Pressure (bar)	2.0	2.0	2.0	Fixed
Reynolds (-)	34 – 493	0.4 – 5.5	1.5 – 21.3	Output of the model
Cooling tubes				
Length (m)	4.0	5.0	15.0	Design criteria (Section 3.2)
Inner diameter (m)	0.02	0.02	0.02	Design criteria (Section 3.2)
Number of tubes (-)	1	187	2,705	Design criteria (Section 3.2)
CO_2 mass inlet (total) (kg/s)	0.0121	2.32	127.4	Output of the model (fixed $T_{cf,0}$)
Recovered heat (MW)	0.0076	1.45	79.9	Output of the model
Inlet T (ºC)	100.0	100.0	100.0	Boundary condition
Outlet T (ºC)	650.0	650.0	650.0	Fixed
Pressure (bar)	50.0	50.0	42.8 – 50.0	Output of the model
Reynolds (-)	9,862 – 19,995	10,098 – 20,476	38,411 – 77,804	Output of the model

The CaO conversion and temperature profiles along the reactor are preserved at the different scales (Fig. 11). At pilot scale (multi-tube reactor), the convective coefficient diminishes one order of magnitude in the reactants side; i.e. shell side. Therefore, the reactor has to be extended 1 meter in length (from 4 m in single tube to 5 meter in multi-tube) in order to bring the products again to 850 ºC and thus recover their sensible heat. Otherwise, part of the exothermal heat from carbonation would not be recovered in the reactor.

Besides, when following the criteria of constant L/v and L/d ratios to pass from mid to large scale, the mass of cooling fluid per tube has to be increased to maintain its exit temperature at 650 ºC. Doing so, the length of the reactor can be shortened to 15 m (instead of the 19 m that would result from the L/d restriction). The final configuration is suitable for a large-scale carbonation, in terms of operating temperature (average 850.6 ºC, computed as $\sum_{i=1}^{100} T_{Li}/100$), residence time (6.5 – 7.5 s) and dimensions (15 m length and 3.3 m diameter).

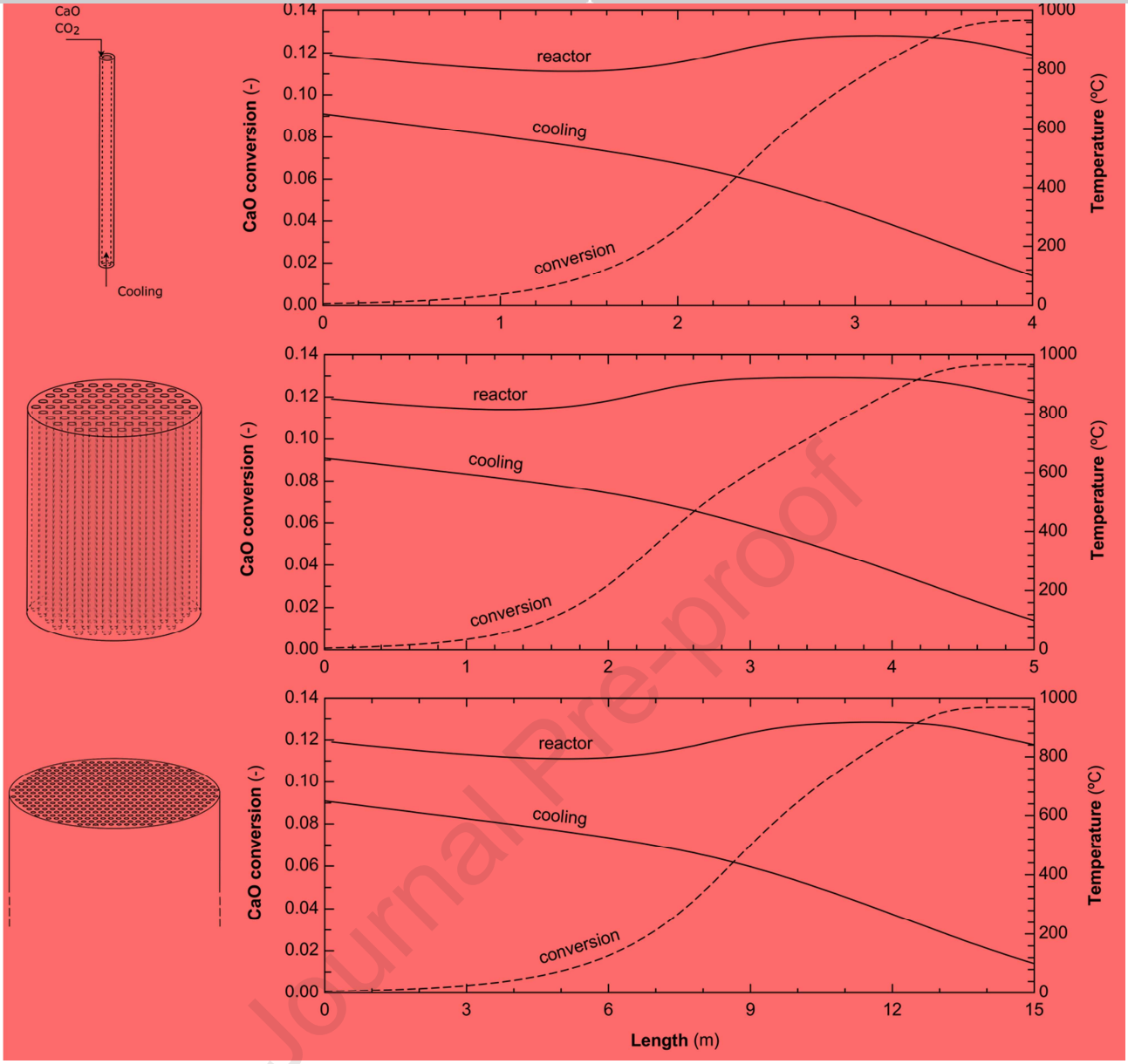

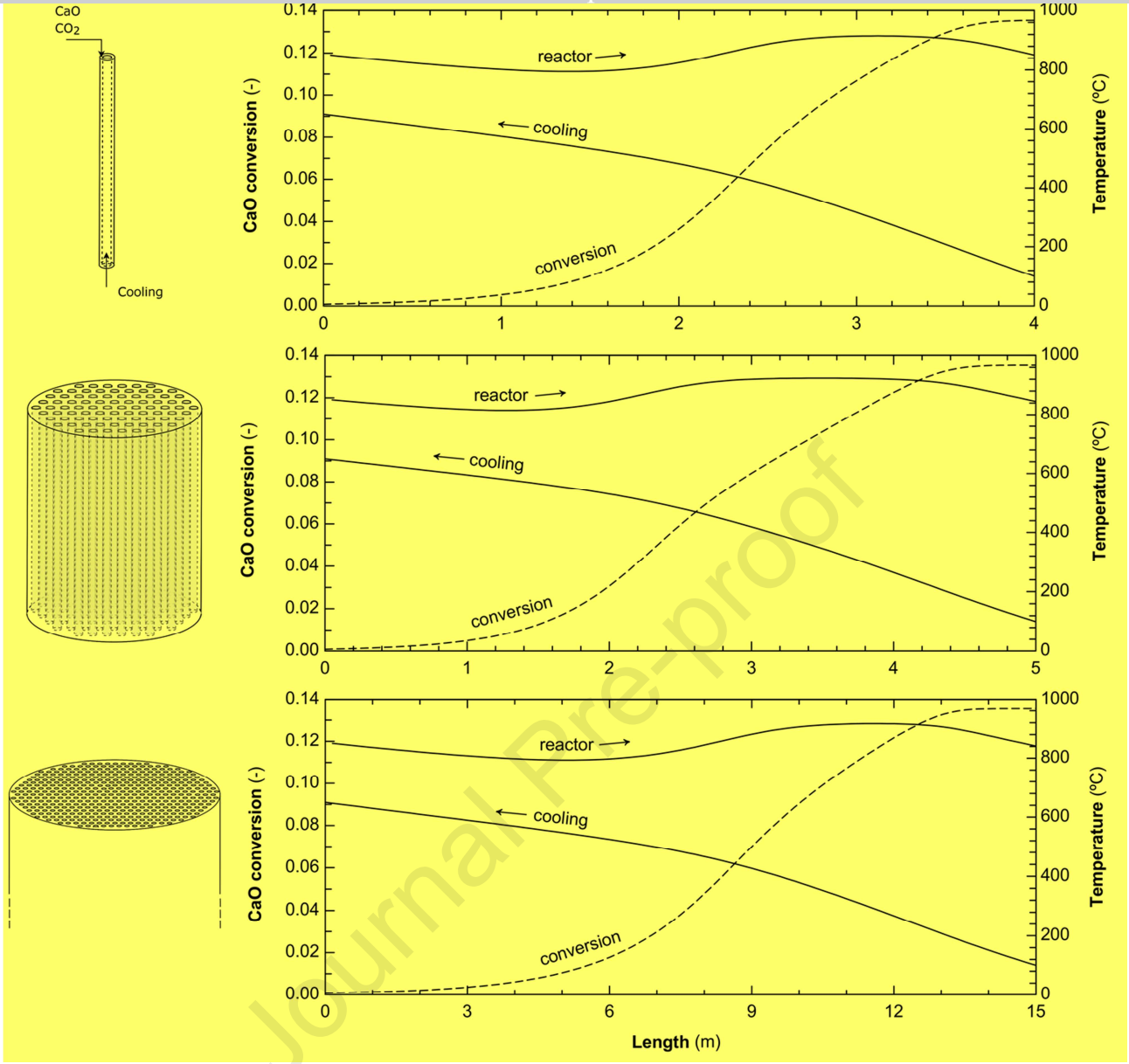

Fig. 11. CaO conversion and temperature profiles (reactor and cooling sides) vs. length (from top to bottom) for the single-tube, multi-tube and large-scale multi-tube configurations. Profiles are kept similar at the different scales (arrows depict the direction of the flow).

Once the reactor at large-scale is defined, partial load operation is assessed (the part load in the carbonator is defined as the ratio between the input mass flow and the nominal input mass flow). Reducing the load in the carbonator means that the inlet mass flowrates of reactants are proportionally reduced, so the available exothermal heat from carbonation will diminish. Therefore, the amount of cooling fluid that can be heated diminishes (always keeping its exit temperature at 650 ºC). The definition of minimum partial load of the reactor corresponds with the point in which the cooling mass flowrate is reduced to the half of its nominal value; i.e. the minimum flowrate of cooling fluid will be 63.7 kg/s of CO_2 at 650 ºC (below this mass flow we assumed that the coupling with the power block cannot longer take place) [40]. This point corresponds to a partial load of 23.9% in the carbonator (Fig. 12) (only the 23.9% of the nominal input flow of CO_2 and CaO is entering the carbonator).

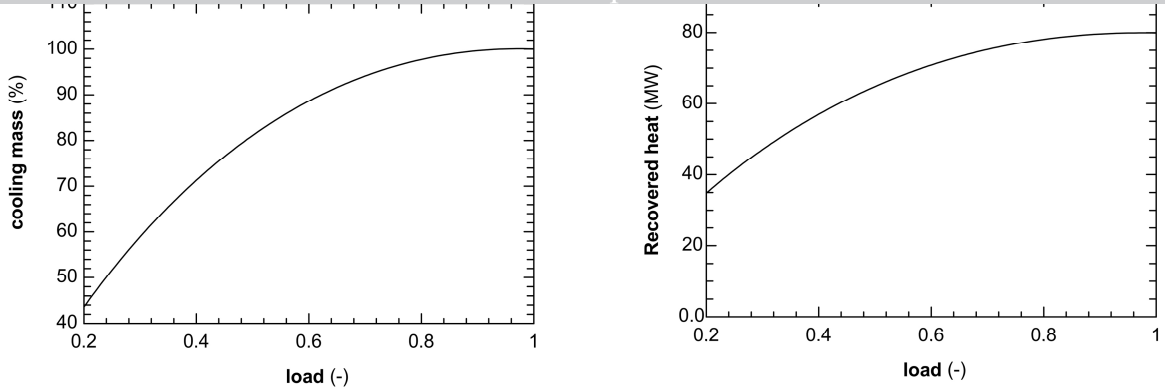

Fig. 12. Cooling mass flow and recovered heat vs. operating load (ratio between the input mass flow in the carbonator and its nominal input mass flow) for the large-scale multi-tube. Outlet temperature of cooling fluid is kept at 650 ºC.

When load is reduced, the volume of reactants is lowered and so does their velocity throughout the reactor. The reaction ends earlier, and the cooling fluid starts recovering sensible heat from the products. Fig. 13 illustrates this fact for a 50% partial load. Thus, the total recovered heat does not diminish linearly with part load (see Fig. 12), and follows Eq. (71) when fitted to a polynomial expression by the least squares method.

$$\dot{Q}_c = 3.27 + 184.5 \cdot \text{load} - 137.8 \cdot \text{load}^2 + 30.0 \cdot \text{load}^3 \quad (71)$$

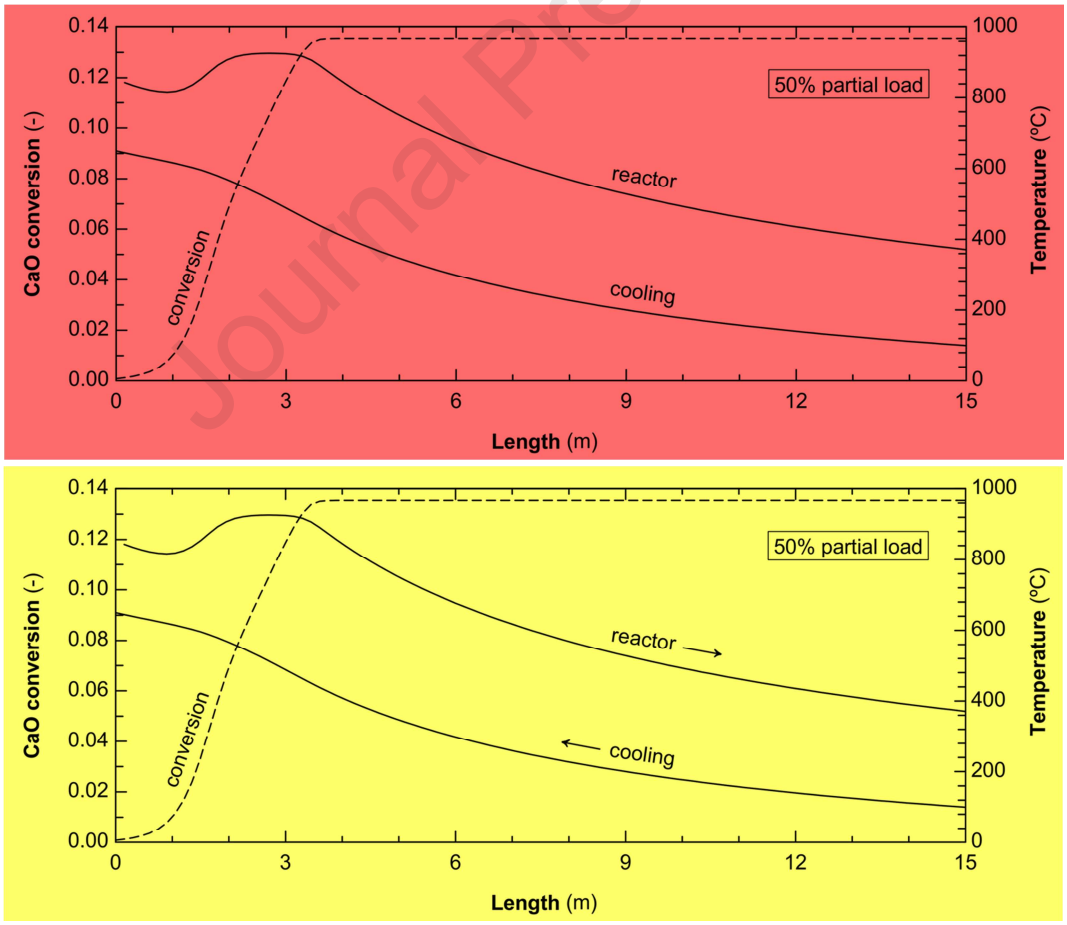

Fig. 13. CaO conversion and temperature profiles vs. length (from top to bottom) for the large-scale multi-tube at 50% partial load (arrows depict the direction of the flow).

4.3. Plant management and size of storages

The distribution of storage and discharge fractions versus carbonator and calciner loads are shown in Fig. 14. Under energy storage mode, the storage fraction of the lime ($f_{st,CaO}$) and CO_2 ($f_{st,CO2}$) is maximum for those operating regions in which the load of the calciner is high while the load of the carbonator is low. In the same way, the $CaCO_3$ discharge fraction ($f_{dch,CaCO3}$) from its storage tank increases from 0 to 1 if the calciner load rises and the carbonator load is reduced. However, since the minimum partial load of the carbonator is 23.9% according to our design, the maximum storage fraction of lime and CO_2 and the maximum discharge fraction of $CaCO_3$ will be 0.761. Regarding the release operation mode, the discharge fraction of the lime ($f_{dch,CaO}$) and CO_2 ($f_{dch,CO2}$) from storage tanks is maximum for operating points with low calciner and high carbonator loads. Likewise, the storage fraction of the $CaCO_3$ ($f_{st,CaCO3}$) obtained through carbonation increases from 0 to 1 if the calciner load is reduced and the carbonator load rises. These storage and discharge fractions operation maps are useful to establish how to operate the plant and manage the storage.

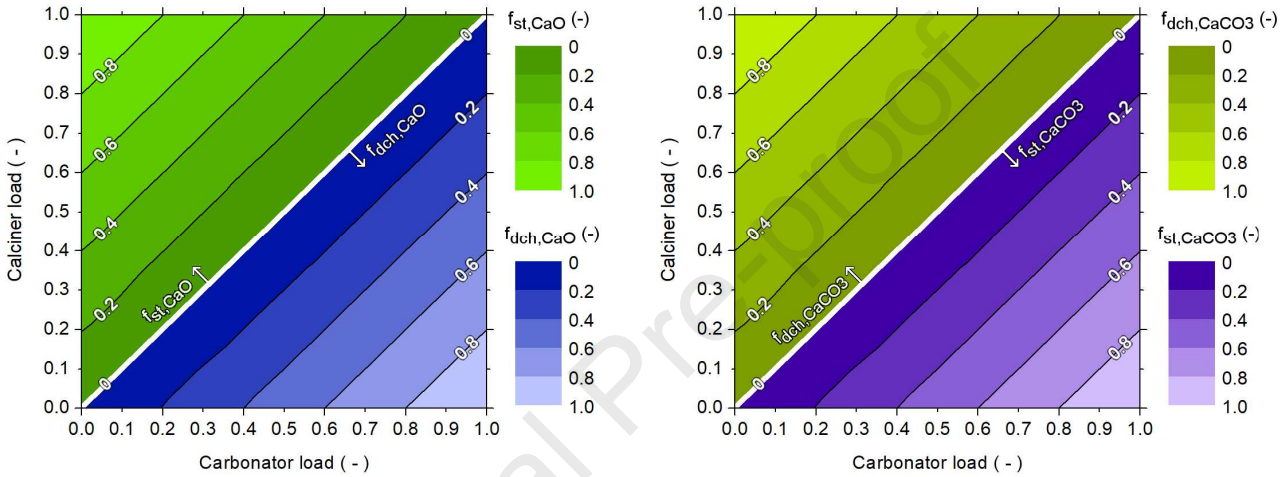

Fig. 14. Storage and discharge fractions operation map.

The maximum storage flowrates of CO_2, CaO and limestone are illustrated in Fig. 15 (assuming 0 void fraction inside the tanks of the solids). The maximum storage volumes are obtained applying Eq. (70) when solar calciner operates at nominal load and carbonator operates at its minimum operation load. The CaO density considered to calculate the volumetric flowrate is 1800 kg/m^3, the density of $CaCO_3$ is 2710 kg/m^3, and the void fraction inside the tank is 30% [41]. Tank sizes ranges from 330 to 514 m^3 for one hour of storage operation, and up to 5,700 – 11,400 m^3 for 15 hours. In the latter case, the storing volume required is 8,256 m^3 for CO_2 in gas phase, 5,824 m^3 for CaO and 7,926 m^3 for the mixture of CaO-$CaCO_3$.

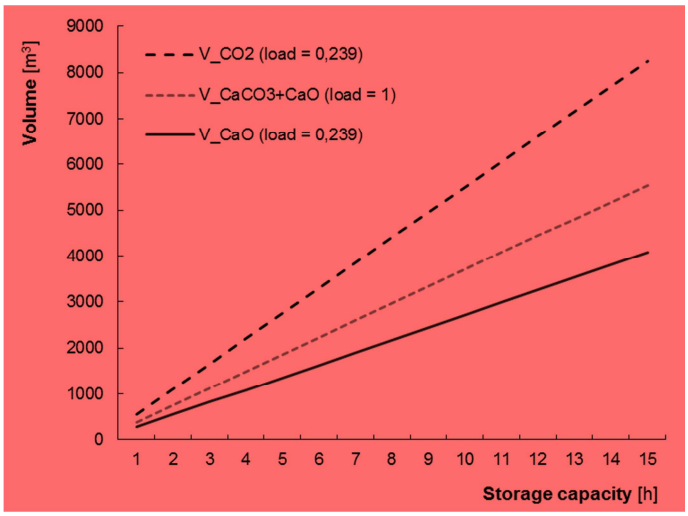

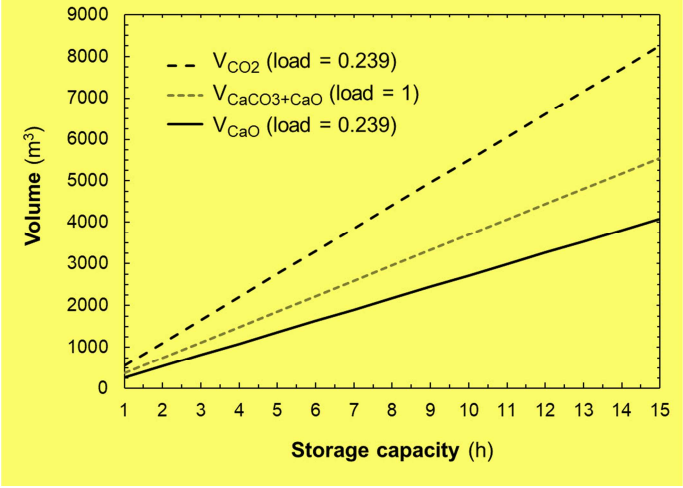

Fig. 15. Maximum storage tanks volumes for different storing timeframes (ideal case with 0 void fraction inside the tank).

It should be noted that, when stored, the apparent density of a solid material is reduced due to the void space between particles. In a randomly packed bed of spheres, the apparent density can be reduced up to 60% [41]. This effect has not been taken into account in the data presented in Fig. 15, but it has been considered in the data presented in the text.

4.4. Overall efficiency of the plant at part load

The efficiencies defined to characterize the plant operation present differences between the energy storage mode and discharge mode. Under energy storage mode, the specific storage consumption (Eq. (62)) has been calculated for each possible pair of carbonator/calciner loads, ranging from 770 MJ/t_{CaO} to 1324 MJ/t_{CaO}. The minimum specific storage consumption corresponds to high carbonator load, while the maximum value refers to operating points in which carbonator reactor is shut-down.

The specific storage consumption is related to the energy storage efficiency. The distribution of the energy storage efficiency versus carbonator and calciner loads is shown in Fig. 16. The maximum storage efficiency (76%) is obtained when the solar calciner operates at nominal load and the carbonator load is 90%, which corresponds to the minimum specific storage consumption. The lower is the storage of CaO and CO_2, the lower is the energy consumed in the energy storage process.

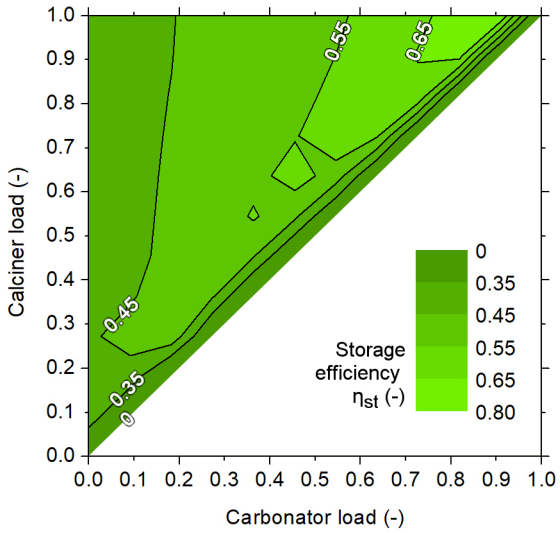

Fig. 16. Storage efficiency operation map.

The carbonator efficiency as a function of the carbonator and calciner loads is illustrated in Fig. 17. The carbonator efficiency is clearly differentiated according to the operating mode in which the system is located (storage or release). For each possible pair of carbonator/calciner loads, the carbonator efficiency is obtained applying Eq. (68) if there is energy discharge and Eq. (64) if there is energy storage. Under energy release mode, the carbonator efficiency is reduced for high carbonator and low calciner loads. This occurs because the energy released in the carbonator in that case comes mainly from the tanks (i.e., it is energy that was previously stored). The minimum carbonator efficiency is 20%, which corresponds to the operating point of the maximum energy demand without solar energy available. Regarding energy storage mode, the carbonator efficiency is greater for low calciner and carbonator loads. This occurs because the energy required from the system to release energy in the carbonator is reduced. Theoretically, the maximum carbonator efficiency is 84%, which corresponds to the operating point with a carbonator load of 10% and a calciner load of 20%. However, since the minimum partial load of the carbonator is 23.9% according to our technical design, the maximum carbonator efficiency will be 81%. This corresponds to the operating point with carbonator load of 23.9% and calciner load of 30%. On the other hand, if there is no storage or discharge of energy (i.e., all the energy received in the calciner is directed to the carbonator), the maximum carbonator efficiency (85%) is obtained with carbonator and calciner loads of 23.9%.

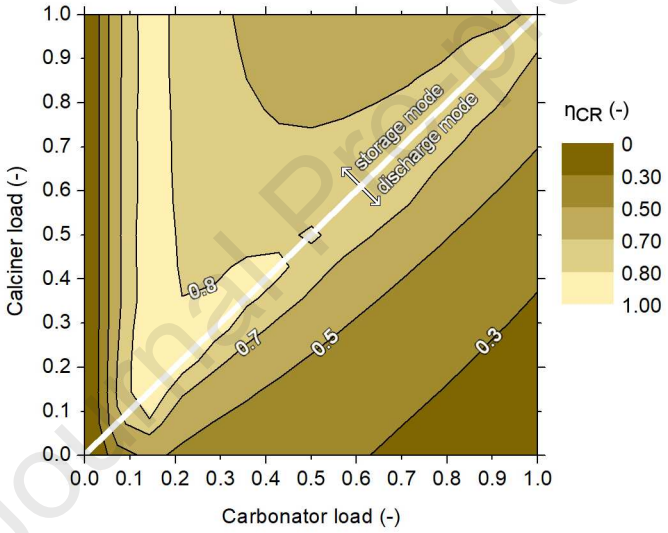

Fig. 17. Carbonator efficiency operation map.

The available energy efficiency of the system as a function of the carbonator and calciner loads is illustrated in Fig. 18. For each pair of carbonator/calciner loads, the available energy efficiency is computed by Eq. (69) when energy discharge takes place and by Eq. (65) when energy is stored. Under energy release mode, the available energy efficiency diminishes at high carbonator and low calciner loads because the energy required by the overall system to produce available energy increases. The minimum available energy efficiency is 55%, which corresponds to the operating point of the maximum energy demand without solar energy available. Regarding energy storage mode, the available energy efficiency increases with energy demand. Theoretically, the maximum available efficiency is 91%, which corresponds to the operating point in which the carbonator load is 20% and the calciner load is 23.9%. However, since the minimum partial load of the carbonator is 23.9% due to technical reasons, the maximum available energy efficiency will be limited to 90%, with a carbonator load of 23.9% and a calciner load of 30%. Besides, in those cases in which all the energy received in the calciner is directed to the carbonator (there is no release or storage), the maximum available energy efficiency (97%) is obtained with carbonator and calciner loads of 23.9%. Actually, the highest available energy efficiencies are achieved around the operation points in which the circulation of mass flow between calciner and carbonator is almost direct (i.e., either the storage is minimal or the energy discharge is negligible).

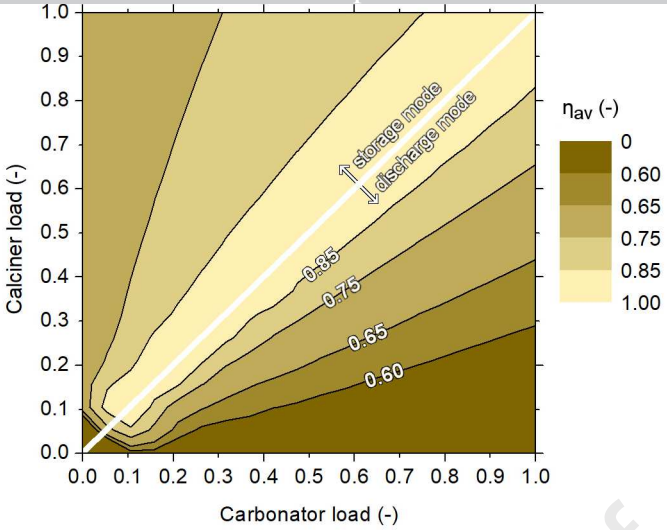

Fig. 18. Available energy efficiency operation map.

5. Conclusions

Two main research gaps were identified in the existing studies of CaL as TCES for CSP: (i) a specific design of large-scale carbonator and (ii) an overall concept analysis accounting the influence of the reactor design on the available heat and the part load operation. Thus, a detailed entrained flow carbonator model was developed to support the scaling-up and design process of a large-scale carbonator. The final industrial design (15 m in length and 3.3 m in diameter) is able to process 187.6 kg/s of CaO and 20.8 kg/s of CO_2 at nominal load, typically operating at 850 ºC and 2 bar. It is observed that the carbonation behavior at large scale can be similar to the behavior at small scale; with residence times of 6.5 – 7.5 s and outlet CaO conversion of 13.5%.

The heat removed from the carbonator through internal cooling tubes (127.4 kg CO_2 with 650 ºC outlet temperature) amounts to 80 MWth and is diverted to the power cycle. The minimum part load of the carbonator is achieved for 23.9% of nominal inlet reactants flows. The available heat at this minimum load is 40 MWth since, besides the heat from the carbonation reaction, part of the sensible thermal energy of the reactor is recovered.

In terms of plant management, useful operation maps were obtained to size and manage the storage tanks of the CaL products. To store energy during 15 hours of operation in a 100 MWth solar power plant, the required CO_2 tank volume is 8,256 m^3, the CaO tank 5,824 m^3 and the CaO-$CaCO_3$ tank 7,926 m^3. The specific energy demand of storage process ranges between 770 and 1324 MJ/t_{CaO}, depending on the calciner and carbonator load. The maximum storage efficiency is 76%.

The carbonator efficiency was mapped versus the calciner and carbonator loads. The highest carbonator efficiencies (80 – 81%) were obtained at low partial loads. Under release operating mode, the lowest carbonator efficiencies (20 – 30%) are found for (high-low) values of the pair (carbonator load-calciner load). This situation corresponds to high discharge fractions of CaO and CO_2 from the storage tanks and presents a significant energy demand for their preheating. Under energy storage operation mode, the influence of partial loads on the carbonator efficiency is softer since energy demand for solid preheating plays a minor role in the whole energy balance.

Lastly, the available energy efficiency was calculated (55 to 97%) and a quite similar behaviour for both operation modes was observed. This efficiency is higher when the part loads of both reactors (calciner and carbonator) are similar since lower mass flows have to be discharged and preheated from the storage tanks.

Future research should focus on the energy optimization of the system, the design and sizing of the equipment involved (heat exchangers, calciner, compression-refrigeration train for CO_2 storage, etc.) and the selection of technically feasible operating points under transient operation modes.

Acknowledgments

The research leading to these results has received funding from the European Union's Horizon 2020 research and innovation programme under grant agreement No 727348, project SOCRATCES. The FPU Programme of the Spanish Ministry of Science, Innovation and Universities (FPU 2017/03902) provided financial support for Sara Pascual during her Ph.D. studies. This work was also supported by the Government of Aragon and co-financed by FEDER 2014-2020 "Construyendo Europa desde Aragón" (Research Group DGA T46_17R).

Nomenclature

Symbols

a_2	pre-exponential factor, 1/s
a	fitting parameter for the equilibrium pressure, K
ā	heat transfer area, m^2
A	specific projection area of the dispersed particles, m^2/kg
A_v	geometry-dependent absorptance of the gas body, -
$\mathcal{A}$	pre-exponential factor, atm
A	calculation parameter, -
b	calculation parameter, 1/s
Cp	specific heat, kJ/(kmol·K)
CS	sensible heat, MW
d, D	diameter, m
E_2	carbonation activation energy, kJ/mol
f	fraction, -
f_p	pressure correction factor, -
fRe_D	friction factor, -
g	gravity, m/s^2
Gz	Graetz number, -
h	convective heat transfer coefficient, $kW/(m^2 \cdot K)$
h	specific enthalpy, kJ/kmol
k	thermal conductivity, kW/(m·K)
K	emission or absorption coefficient of the gas phase, 1/m
ℓ	heat transfer length, m
l_{mb}	mean beam length, m
$load$	carbonator load (ratio between the input mass flow and the nominal input mass flow), -
L	length, m
L_p	particle load at operation conditions, kg/m^3
$\dot{m}$	mass flow rate, kg/s
n	exponent factor, -
$\dot{n}$	mole flow rate, kmol/s
N	number of cooling tubes, -
Nu	Nusselt number (local), -
$\overline{Nu}$	Nusselt number (average), -
O_{Lev}	offset in the extended Lévêque solution, -
per	perimeter, m
P	pressure, bar
Pr	Prandtl number, -
$\dot{q}'$	heat flow per unit of length, kW/m
$\dot{Q}$	rate of heat flow, MW or kW
$\bar{Q}$	mean relative absorption or backscattering efficiency of a particle, -
r	reaction rate, 1/s
r	radius, m
r_*	ratio between inner and outer radius, -
R	molar ratio CaO/CO_2, -
R	thermal resistance, K/kW
Re_D	Reynolds number based on hydraulic diameter, -
$\mathcal{R}$	ideal gas constant, kJ/(kmol·K)
s_{eq}	equivalent layer thickness, m
S_{eff}	effective cross-sectional area of reactor, m^2
SSC	specific storage consumption
t	reacting time or residence time, s
t_0	time to reach half of residual conversion, s
T	temperature, K
v	velocity, m/s
V	volume, m^3
$\dot{V}$	volumetric flow rate, m^3/s
X	conversion, -
X_k	residual conversion, -
ΔL	length of the discretized slice, m
ΔS_2^0	carbonation entropy change, J/(mol·K)
ΔH_2^0	standard enthalpy change of carbonation, kJ/mol
ΔH_r	enthalpy of carbonation, kJ/kmol

Greek symbols

α	absorptivity, -
β	calculation parameter, -

γ calculation parameter, -
ε emissivity, -
η efficiency, -
η_{av} available energy efficiency (ratio between the available heat and the energy invested), -
η_{CR} carbonator efficiency (ratio between the heat recovered and the energy invested), -
η_{st} storage efficiency (ratio between the stored energy and the energy invested), -
λ_1, λ_2 calculation parameter, -
μ viscosity, kg/(m·s)
ρ density, kg/m^3
σ Stefan-Boltzmann constant, kW/(m^2·K^4)
Φ optical thickness for the gas solid dispersion, -

Subscripts and superscripts

abs absorption
av available thermal energy
bsc backscattering
c carbonator
cf cooling fluid / cooling tube
CL in the calciner or for calcination
$conv$ convection
CR in the carbonator or for carbonation
dch discharge
emi emission
eq equilibrium
$EROM$ energy release operation mode
$ESOM$ energy storage operation mode
f fresh
g gas
h hydraulic diameter
i initial value or discretization index for axial position
in inner or inlet
iw wall in contact with the cloud of gas and particles
j component j
L covered length
Li axial position at length L_i from top
max maximum or nominal capacity
out outer radius/diameter or outlet
ow wall in contact with the cooling fluid
p purge or particle
rad radiation
s solid
st storage
t terminal velocity
tb cooling tubes
$tube$ carbonator's tube
w wall
0 initial
∞ fully developed heat transfer

References

[1] Eurostat. Greenhouse gas emissions by sector (source: EEA) (code: tsdcc210) n.d. http://ec.europa.eu/eurostat/web/environment/air-emissions-inventories/main-tables (accessed February 17, 2017).

[2] IEA. World Energy Outlook 2018. International Energy Agency; 2018. doi:10.1787/weo-2018-2-en.

[3] Pierre I, Bauer F, Blasko R, Dahlback N, Dumpelmann M, Kainurinne K, et al. Flexible generation: Backing up renewables. 2011.

[4] European Commission. Commission staff working document: Energy storage – the role of electricity. 2017.

[5] IEA. Status of Power System Transformation 2019. Power system flexibility. International Energy Agency; 2019.

[6] Concentrating Solar Power Projects. National Renewable Energy Laboratory 2018.

[7] Achkari O, El Fadar A. Latest developments on TES and CSP technologies – Energy and environmental issues, applications and research trends. Appl Therm Eng 2020;167:114806. doi:10.1016/j.applthermaleng.2019.114806.

[8] Kearney D, Kelly B, Herrmann U, Cable R, Pacheco J, Mahoney R, et al. Engineering aspects of a molten salt heat transfer fluid in a trough solar field. Energy 2004;29:861–70. doi:10.1016/S0360-5442(03)00191-9.

[9] Mohan G, Venkataraman MB, Coventry J. Sensible energy storage options for concentrating solar power plants operating above 600 °C. Renew Sustain Energy Rev 2019;107:319–37. doi:10.1016/j.rser.2019.01.062.

[10] Letcher TM. Storing Energy: With Special Reference to Renewable Energy Sources. Elsevier Inc.; 2016. doi:10.1515/ci-2016-0627.

[11] Almendros-Ibáñez JA, Fernández-Torrijos M, Díaz-Heras M, Belmonte JF, Sobrino C. A review of solar thermal energy storage in beds of particles: Packed and fluidized beds. Sol Energy 2019;192:193–237. doi:10.1016/j.solener.2018.05.047.

[12] Prieto C, Cabeza LF. Thermal energy storage (TES) with phase change materials (PCM) in solar power plants (CSP). Concept and plant performance. Appl Energy 2019;254:113646. doi:10.1016/j.apenergy.2019.113646.

[13] Prieto C, Cooper P, Fernández AI, Cabeza LF. Review of technology: Thermochemical energy storage for concentrated solar power plants. Renew Sustain Energy Rev 2016;60:909–29. doi:10.1016/j.rser.2015.12.364.

[14] Chen X, Zhang Z, Qi C, Ling X, Peng H. State of the art on the high-temperature thermochemical energy storage systems. Energy Convers Manag 2018;177:792–815. doi:10.1016/j.enconman.2018.10.011.

[15] Khosa AA, Xu T, Xia BQ, Yan J, Zhao CY. Technological challenges and industrial applications of CaCO3/CaO based thermal energy storage system – A review. Sol Energy 2019;193:618–36. doi:10.1016/j.solener.2019.10.003.

[16] Barker R. The Reactivity of Calcium Oxide Towards Carbon Dioxide and Its Use for Energy Storage. J Chem Technol Biotechnol 1974;24:221–7. doi:https://doi.org/10.1002/jctb.2720240405.

[17] Ortiz C, Chacartegui R, Valverde JM, Alovisio A, Becerra JA. Power cycles integration in concentrated solar power plants with energy storage based on calcium looping. Energy Convers Manag 2017;149:815–29. doi:10.1016/j.enconman.2017.03.029.

[18] Tesio U, Guelpa E, Verda V. Integration of ThermoChemical Energy Storage in Concentrated Solar Power. Part 1: energy and economic analysis/optimization. Energy Convers Manag X 2020:100039. doi:10.1016/j.ecmx.2020.100039.

[19] Ortiz C, Romano MC, Valverde JM, Binotti M, Chacartegui R. Process integration of Calcium-Looping thermochemical energy storage system in concentrating solar power plants. Energy 2018;155:535–51. doi:10.1016/j.energy.2018.04.180.

[20] Chacartegui R, Alovisio A, Ortiz C, Valverde JM, Verda V, Becerra JA. Thermochemical energy storage of concentrated solar power by integration of the calcium looping process and a CO2 power cycle. Appl Energy 2016;173:589–605. doi:10.1016/j.apenergy.2016.04.053.

[21] Tesio U, Guelpa E, Verda V. Integration of ThermoChemical Energy Storage in Concentrated Solar Power. Part 2: comprehensive optimization of supercritical CO2 power block. Energy Convers Manag X 2020;6:100038. doi:10.1016/j.ecmx.2020.100038.

[22] Bravo R, Ortiz C, Chacartegui R, Friedrich D. Hybrid solar power plant with thermochemical energy storage: A multi-objective operational optimisation. Energy Convers Manag 2020;205:112421. doi:10.1016/j.enconman.2019.112421.

[23] Zsembinszki G, Sole A, Barreneche C, Prieto C, Fernández AI, Cabeza LF. Review of reactors with potential use in thermochemical energy storage in concentrated solar power plants. Energies 2018;11. doi:10.3390/en11092358.

[24] Koepf E, Alxneit I, Wieckert C, Meier A. A review of high temperature solar driven reactor technology: 25 years of experience in research and development at the Paul Scherrer Institute. Appl Energy 2017;188:620–51. doi:10.1016/j.apenergy.2016.11.088.

[25] Karasavvas E, Panopoulos KD, Papadopoulou S, Voutetakis S. Study of a drop-tube carbonator reactor for CSP-calcium looping based on a heterogeneous reaction model. Chem Eng Trans 2019;76:877–82. doi:10.3303/CET1976147.

[26] Bailera M, Lisbona P, Romeo LM, Díez LI. Calcium looping as chemical energy storage in concentrated solar power plants: Carbonator modelling and configuration assessment. Appl Therm Eng 2020:115186. doi:10.1016/j.applthermaleng.2020.115186.

[27] Rodriguez N, Alonso M, Grasa G, Abanades JC. Heat requirements in a calciner of CaCO3integrated in a CO2capture system using CaO. Chem Eng J 2008;138:148–54. doi:10.1016/j.cej.2007.06.005.

[28] Lisbona P, Martínez A, Lara Y, Romeo LM. Integration of carbonate CO2 capture cycle and coal-fired power plants. A comparative study for different sorbents. Energy and Fuels 2010;24:728–36.

doi:10.1021/ef500740p.

[29] Martínez A, Lara Y, Lisbona P, Romeo LM. Operation of a mixing seal valve in calcium looping for CO2 capture. Energy and Fuels 2014;28:2059–68. doi:10.1021/ef402487e.

[30] Martínez A, Lara Y, Lisbona P, Romeo LM. Energy penalty reduction in the calcium looping cycle. Int J Greenh Gas Control 2012;7:74–81. doi:10.1016/j.ijggc.2011.12.005.

[31] Ortiz C, Valverde JM, Chacartegui R, Perez-Maqueda LA. Carbonation of Limestone Derived CaO for Thermochemical Energy Storage: From Kinetics to Process Integration in Concentrating Solar Plants. ACS Sustain Chem Eng 2018;6:6404–17. doi:10.1021/acssuschemeng.8b00199.

[32] Wen CY, Chaung TZ. Entrainment Coal Gasification Modeling. Ind Eng Chem Process Des Dev 1979;18:684–95. doi:10.1021/i260072a020.

[33] Kabelac S, Vortmeyer D. VDI Heat Atlas Part K - Radiation. In: VDI, editor. VDI Heat Atlas. Second, Springer-Verlag Berlin Heidelberg; 2010.

[34] Nellis G, Klein S. Heat transfer. Cambridge University Press; 2008.

[35] Bennett TD. Exact solutions to the thermal entry problem for laminar flow through annular ducts. J Heat Transfer 2020;142:1–12. doi:10.1115/1.4046345.

[36] Taborek J. Double-pipe and multitube heat exchangers with plain and longitudinal finned tubes. Heat Transf Eng 1997;18:34–45. doi:10.1080/01457639708939894.

[37] Bennett TD. Correlations for the Graetz problem in convection – Part 1: For round pipes and parallel plates. Int J Heat Mass Transf 2019;136:832–41. doi:10.1016/j.ijheatmasstransfer.2019.03.006.

[38] Zlokarnik M. Scale-Up in Chemical Engineering. Wiley-VCH Verlag GmbH & Co. KGaA; 2002.

[39] Plou J, Martínez I, Grasa GS, Murillo R. Experimental carbonation of CaO in an entrained flow reactor. React Chem Eng 2019:899–908. doi:10.1039/c9re00015a.

[40] Taler J, Zima W, Ocłoń P, Grądziel S, Taler D, Cebula A, et al. Mathematical model of a supercritical power boiler for simulating rapid changes in boiler thermal loading. Energy 2019;175:580–92. doi:10.1016/j.energy.2019.03.085.

[41] Song C, Wang P, Makse HA. A phase diagram for jammed matter. Nature 2008;453:629–32. doi:10.1038/nature06981.

- Calcium looping thermochemical energy storage has been modelled at large scale.
- The minimum operating load of carbonator is 23.9% due to technical limitations.
- The available energy efficiency of the overall system is in the range 55 – 97%.
- The require size to store CaO and $CaCO_3$ solids during 15 h is 5,700 – 11,400 m^3.

Declaration of interests

☒ The authors declare that they have no known competing financial interests or personal relationships that could have appeared to influence the work reported in this paper.

☐The authors declare the following financial interests/personal relationships which may be considered as potential competing interests: